DIFFUSION TRANSFORMERS WITH REPRESENTATION AUTOENCODERS

Anonymous authors
Paper under double-blind review

ABSTRACT

Latent generative modeling has become the standard strategy for Diffusion Transformers (DiTs), but the autoencoder has barely evolved. Most DiTs still use the legacy VAE encoder, which introduces several limitations: large convolutional backbones that compromise architectural simplicity, low-dimensional latent spaces that restrict information capacity, and weak representations resulting from purely reconstruction-based training. In this work, we investigate replacing the VAE encoder–decoder with pretrained representation encoders (e.g., DINO, SigLIP, MAE) combined with trained decoders, forming what we call *Representation Autoencoders* (RAEs). These models provide both high-quality reconstructions and semantically rich latent spaces, while allowing for a scalable transformer-based architecture. A key challenge arises in enabling diffusion transformers to operate effectively within these high-dimensional representations. We analyze the sources of this difficulty, propose theoretically motivated solutions, and validate them empirically. Our approach achieves faster convergence without auxiliary representation alignment losses. Using a DiT variant with a lightweight wide DDT-head, we demonstrate state-of-the-art image generation performance, reaching FIDs of 1.18 @256 resolution and 1.13 @512 on ImageNet.

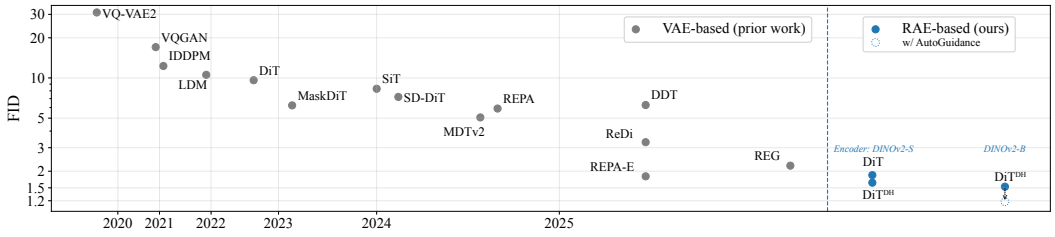

Figure 1: Representation Autoencoder (RAE) uses frozen pretrained representations as the encoder with a lightweight decoder to reconstruct input images without compression. RAE enables faster convergence and higher-quality samples in latent diffusion training compared to VAE-based models.

1 INTRODUCTION

Diffusion models have rapidly become the dominant paradigm for image generation. A key factor in their success is the use of latent generative modeling (Rombach et al., 2022), where the diffusion process is carried out not on pixels but within the compressed latent space of a Variational Autoencoder (VAE) (Kingma & Welling, 2014). By working in latents, diffusion models can achieve both higher sample quality and greater computational efficiency compared to pixel-space counterparts. Since the advent of Diffusion Transformer (DiT) (Peebles & Xie, 2023), the combination of DiT and latent diffusion modeling has emerged as the standard recipe for scalable generative modeling (Esser et al., 2024; Liu et al., 2024; Tong et al., 2025; Labs, 2024; Pan et al., 2025).

Despite this progress in diffusion backbone, the VAE widely used today still largely follow the recipe introduced by Stable Diffusion (SD-VAE) (Rombach et al., 2022), whose design poses many limitations. First, its heavily compressed latent space restricts information capacity: the higher the compression, the poorer the reconstruction quality (Yao et al., 2025). Second, aggressive compression combined with the exclusive use of reconstruction objectives yields weak latent representations. For this, recent works have incorporated multiple representation-supervision objectives to enhance

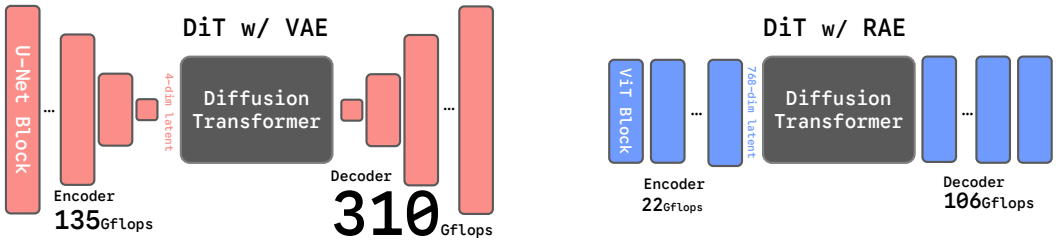

Figure 2: **Comparison of SD-VAE and RAE (DINOv2-B).** The VAE relies on convolutional backbones with aggressive down- and up-sampling, while the RAE uses a ViT architecture *without* compression. SD-VAE is also more computationally expensive, requiring about 6× and 3× more GFLOPs than RAE for the encoder and decoder, respectively. GFlops are evaluated on one 256×256 image.

VAE performance. For instance, VA-VAE (Yao et al., 2025) aligns VAE latents with a pretrained representation encoder, while MAETok (Chen et al., 2025a), DC-AE 1.5 (Chen et al., 2025d), and l-DEtok (Yang et al., 2025) integrate mask- or noise-augmented objectives into VAE training. Together, these studies highlight the critical role of representation quality in autoencoder design.

In this work, we raise a simple yet fundamental question: what if we replaced the legacy VAE with modern representation learning encoders? The wave of pretrained vision models such as DINOv2 (Caron et al., 2021a), SigLIP (Tschannen et al., 2025), and MAE (He et al., 2021) demonstrates that large-scale representation learning yields semantically rich features. We show that we can repurpose these **frozen** pretrained encoders into autoencoders, which we term **Representation Autoencoders (RAEs)**. With a lightweight learned decoder, RAEs achieve great reconstruction quality on par with SD-VAE while retain strong representational capability.

The benefits of RAEs come with the challenges of high-dimensional latent spaces. On 256×256 images, SD-VAE and RAEs with DINOv2-B produce the same number of tokens, but each RAE token has 768 dimensions—eight times larger than SD-VAE. **Diffusing directly in this space is difficult:** training the same DiT model with RAEs lags significantly behind VAEs. We identify three main causes for this gap: (1) **Transformer design:** we show analytically that DiTs can fail to fit even a single image unless their width exceeds the token dimension, implying the model width must scale with latent dimensionality. (2) **Noise scheduling:** we find that the resolution-dependent schedule shifts in (Chen, 2023; Hoogeboom et al., 2023; Esser et al., 2024), derived from pixel- and VAE-based inputs, overlook the increased token dimensionality. We therefore generalize the schedule shift to be full dimension-dependent (3) **Decoder robustness:** unlike VAEs trained on continuous latent distributions (Kingma & Welling, 2014), RAE decoders learn from discretely supported latents but must reconstruct samples from a diffusion model that follow a continuous distribution, which we address by noise-augmented decoder training.

With these changes, we observe substantial improvements in both generation quality and convergence speed for DiT-XL trained on RAE with DINOv2-B. With only 80 training epochs, DiT-XL achieves an FID of **4.28** @ 256 resolution without guidance, outperforming most diffusion baselines trained with SD-VAE (Peebles & Xie, 2023; Ma et al., 2024; Yu et al., 2025; Yao et al., 2025).

To alleviate the quadratic cost of scaling the entire DiT backbone, we introduce the DDT head—a wide, shallow transformer module dedicated to denoising, inspired by DDT (Wang et al., 2025c). This augmented architecture, **DiT$^{\text{DH}}$**, provides sufficient width without enlarging the backbone and converges much faster than standard DiT with RAE.

DiT$^{\text{DH}}$ pushes the generation capability of diffusion on RAE even further. Using DiT$^{\text{DH}}$-XL on DINOv2-B, we improve the FID to **2.16** @ 256 resolution without guidance at 80 epochs, demonstrating a 10× training speedup compared to baselines such as VA-VAE (Yao et al., 2025) and REPA (Yu et al., 2025). With longer training, DiT$^{\text{DH}}$-XL reaches an unguided FID of **1.53** within 800 epochs. Combining with AutoGuidance (Karras et al., 2025) pushes DiT$^{\text{DH}}$-XL's final FID scores to **1.18** @ 256 and **1.13** @ 512 resolutions, establishing a new state-of-the-art.

2 Related Works

Here, we discuss previous work on the line of representation learning and reconstruction/generation. We present a more detailed related work discussion in Appendix B.

Representation for Reconstruction. Recent work explores enhancing VAEs with semantic representations: VA-VAE (Yao et al., 2025) aligns VAE latents with a pretrained representation encoder, while MAETok (Chen et al., 2025a), DC-AE 1.5 (Chen et al., 2025d), and l-DEtok (Yang et al., 2025) incorporate MAE- or DAE (Vincent et al., 2008)-inspired objectives into VAE training. Such alignment improves reconstruction and generation, but still depends on heavily compressed latents, which limits both fidelity and representation quality. In contrast, we reconstruct directly from representation encoders features without compression. We show that, with a simple ViT decoder on top of frozen representation encoders features, it achieves reconstruction quality comparable to or better than SD-VAE (Rombach et al., 2022), while preserving substantially stronger representations.

Representation for Generation. Recent work also explores using semantic representations to improve generative modeling. REPA (Yu et al., 2025) accelerates DiT convergence by aligning its middle block with representation encoders features. DDT (Wang et al., 2025c) further improves convergence by decoupling DiT into an encoder–decoder and applying REPAlign on the encoder output. REG (Wu et al., 2025) introduces a learnable token into the DiT sequence and explicitly aligns it with a representation encoders representation. ReDi (Kouzelis et al., 2025b) generates both VAE latents and PCA components of DINOv2 features within a diffusion model. In contrast, we train diffusion models directly on representation encoders and achieve faster convergence.

3 High Fidelity Reconstruction from Frozen representation encoders

In this section, we challenge the common claim that pretrained representation encoders, such as DINOv2 (Oquab et al., 2023) and SigLIP2 (Tschannen et al., 2025), are unsuitable for the reconstruction task because they "emphasize high-level semantics while downplaying low-level details" (Tang et al., 2025b; Yu et al., 2024b). We show that, with a suitable decoder, frozen representation encoderss can in fact serve as strong encoders for the diffusion latent space. Our **Representation Autoencoders (RAEs)** pair frozen, pretrained representation encoderss with a ViT-based decoder, yielding reconstructions on par with or even better than SD-VAE. More importantly, RAEs alleviate the fundamental limitations of VAEs (Kingma & Welling, 2014), whose heavily compressed latent space (e.g., SD-VAE maps 256^2 images to $32^2 \times 4$ (Esser et al., 2021; Rombach et al., 2022)) restricts reconstruction fidelity and more importantly, representation quality.

We train RAEs by fixing a pretrained representation encoders and only learning a ViT decoder to reconstruct images from its outputs. For an input $\mathbf{x} \in \mathbb{R}^{3\times H\times W}$ and a ViT encoder E with patch size p_e and hidden size d, we obtain $N = HW/p_e^2$ tokens with channel d. A ViT decoder D with patch size p_d maps them back to pixels with shape $3 \times H\frac{p_d}{p_e} \times W\frac{p_d}{p_e}$; By default we use $p_d = p_e$, so the reconstruction matches the input resolution. For all experiments on 256×256 images, the encoder produces 256 tokens, matching the token count of most prior DiT-based models trained on SD-VAE (Peebles & Xie, 2023; Yu et al., 2025; Ma et al., 2024). We **freeze** the pretrained encoder E and train only the decoder D, using a combination of L1, LPIPS (Zhang et al., 2018), and adversarial losses (Goodfellow et al., 2014), following common practice in VAEs. More details about the decoder architecture and training are provided in Appendix E.

We select three representative encoders from different pretraining paradigms: DINOv2-B (Oquab et al., 2023)(p_e=14, d=768), a self-supervised self-distillation model; SigLIP2-B (Tschannen et al., 2025)(p_e=16, d=768), a language-supervised model; and MAE-B (He et al., 2021)(p_e=16, d=768), a masked autoencoder. For DINOv2, we also study different model sizes S,B,L (d=384,768,1024). Unless otherwise specified, we use an ViT-XL decoder for all RAEs. We evaluate the rFID-50k on ImageNet (Russakovsky et al., 2015) validation set as our main metric for reconstruction quality.

Reconstruction, scaling, and representation. As shown in Table 1a, RAEs with frozen encoders achieve consistently better reconstruction quality (rFID) than SD-VAE. For instance, RAE with MAE-B/16 reaches an rFID of 0.16, clearly outperforming SD-VAE and challenging the assumption that representation encoders cannot recover pixel-level detail.

We next study the scaling behavior of both encoders and decoders. As shown in Table 1c, reconstruction quality remains stable across DINOv2-S, B, and L, indicating that even small representation encoders models preserve sufficient low-level detail for decoding. On the decoder side (Table 1b),

Model	rFID
DINOv2-B	0.49
SigLIP2-B	0.53
MAE-B	0.16
SD-VAE	0.62

(a) **Encoder choice.** All encoders outperform SD-VAE.

Decoder	rFID	GFLOPs
ViT-B	0.58	22.2
ViT-L	0.50	78.1
ViT-XL	0.49	106.7
SD-VAE	0.62	310.4

(b) **Decoder scaling.** Scaling decoders improve rFID, while still being efficient than VAE.

Encoder	rFID
DINOv2-S	0.52
DINOv2-B	0.49
DINOv2-L	0.52

(c) **Encoder scaling.** rFID is stable across RAE sizes.

Model	Top-1 Acc.
DINOv2-B	84.5
SigLIP2-B	79.1
MAE-B	68.0
SD-VAE	8.0

(d) **Representation quality.** RAE has much higher linear probing accuracy than VAE.

Table 1: RAEs consistently outperform SD-VAE in reconstruction (rFID) and representation quality (linear probing accuracy) on ImageNet-1K, while being more efficient. If not specified, we use ViT-XL as the decoder and DINOv2-B as the encoder for RAE. Default settings are marked in gray.

increasing capacity consistently improves rFID: from 0.58 with ViT-B to 0.49 with ViT-XL. Importantly, ViT-B already outperforms SD-VAE while being $14\times$ more efficient in GFLOPs, and ViT-XL further improves quality at only one-third of SD-VAE's cost.

We also evaluate representation quality via linear probing on ImageNet-1K in Table 1d. Because RAEs use frozen pretrained encoders, they directly inherit the representation of the underlying representation encoders. In contrast, SD-VAE achieves only $\sim$8% accuracy.

4 Taming Diffusion Transformers for RAE

With RAE demonstrating good reconstruction quality, we now proceed to investigate the diffusability of its latent space (Skorokhodov et al., 2025); that is, how easily its latent distribution can be modeled by a diffusion model, and how good the generation performance can be. Among MAE, SigLIP2, and DINOv2, we find that DINOv2 achieves the best generation performance (Appendix H.1) and use it as the default encoder for RAE unless otherwise specified.

Following the *de facto* practice, we adopt the rectified flow objective (Lipman et al., 2023; Liu et al., 2023) with linear interpolation $\mathbf{x}_t = (1-t)\mathbf{x} + t\boldsymbol{\varepsilon}$, where $\mathbf{x} \sim p(\mathbf{x})$ and $\boldsymbol{\varepsilon} \sim \mathcal{N}(0, \mathbf{I})$, and train the model to predict the velocity $v(\mathbf{x}_t, t)$ (see Appendix I). We use LightningDiT (Yao et al., 2025), a variant of DiT (Peebles & Xie, 2023), as our model backbone. We primarily evaluate our models using FID (Heusel et al., 2017) computed on 50K samples generated with 50 steps of Euler sampler, and all quantitative results are trained for 80 training epochs on ImageNet@256 unless otherwise specified. More training details are included in Appendix F.

DiT doesn't work out of box. To our surprise, such standard diffusion recipe fails with RAE. Training directly on RAE latents causes a small backbone such as DiT-S to completely fail, while a larger backbone like DiT-XL significantly underperforms compared to its performance on SD-VAE latents.

	RAE	SD-VAE
DiT-S	215.76	**51.74**
DiT-XL	23.08	**7.13**

Table 2: **DiT struggles to model RAE's latent distribution.**

To investigate this failure, we raise several hypotheses detailed below, which we will discuss in the following sections:

- **Suboptimal design for Diffusion Transformers.** When modeling high-dimensional RAE tokens, the optimal design choices for Diffusion Transformers can diverge from those of the standard DiT, which was originally tailored for low-dimensional VAE tokens.
- **Suboptimal noise scheduling.** Prior noise scheduling and loss re-weighting tricks are derived for image-based or VAE-based input, and it remains unclear if they transfer well to high-dimension semantic tokens.
- **Diffusion generates noisy latents.** VAE decoders are trained to reconstruct images from noisy latents, making them more tolerant to small noises in diffusion outputs. In contrast, RAE decoders are trained on only clean latents and may therefore struggle to generalize.

4.1 Scaling DiT Width to Match Token Dimensionality

To better understand the training dynamics of Diffusion Transformers with RAE latents, we first construct a simplified experiment. Rather than training on the entire ImageNet, we randomly select a single image, encode it by RAE, and test whether the diffusion model can reconstruct it.

Table 2 shows that although RAE underperforms SD-VAE, DiT performance improves with increased capacity. To dissect this effect, we vary model width while fixing depth. Starting from

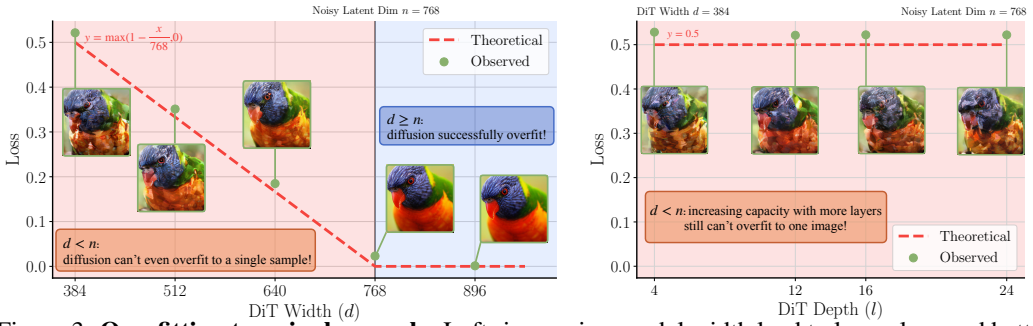

Figure 3: **Overfitting to a single sample.** Left: increasing model width lead to lower loss and better sample quality; Right: changing model depth has marginal effect on overfitting results.

DiT-S, we increase the hidden dimension from 384 to 784. As shown in Figure 3, sample quality is poor when the model width $d < n = 768$, but improves sharply and reproduces the input almost perfectly once $d \geq n$. Training losses exhibit the same trend, converging only when $d \geq n$.

One might suspect that this improvement still arises from the larger model capacity. To disentangle this effect, we fix the width at $d = 384$ and vary the depth of the SiT-S model. As shown in Figure 3, even when the depth is increased from 12 to 24, the generated images remain artifact-heavy, and the training losses shown in Figure 3 fail to converge to similar level of $d = 768$.

Taken together, these results indicate that successful generation in RAE's latent space requires the diffusion model's width to be at least as large as RAE's token dimension. In the following, we provide a theoretical justification for this requirement.

In the following, we provide a theoretical justification for this requirement.

Theorem 1. *Assuming $\mathbf{x} \sim p(\mathbf{x}) \in \mathbb{R}^n, \boldsymbol{\varepsilon} \sim \mathcal{N}(0, \mathbf{I}_n)$, $t \in [0, 1]$. Let $\mathbf{x}_t = (1-t)\mathbf{x} + t\boldsymbol{\varepsilon}$, consider the function family*

$$\mathcal{G}_d = \{g(\mathbf{x}_t, t) = \boldsymbol{B} f(\boldsymbol{A}\mathbf{x}_t, t) : \boldsymbol{A} \in \mathbb{R}^{d \times n}, \boldsymbol{B} \in \mathbb{R}^{n \times d}, f : [0,1] \times \mathbb{R}^d \to \mathbb{R}^d\} \tag{1}$$

*where $d < n$, f refers to a stack of standard DiT blocks whose width is smaller than the token dimension from the representation encoder, and $\boldsymbol{A}, \boldsymbol{B}$ denote the input and output linear projections, respectively. Then for **any** $g \in \mathcal{G}_d$,*

$$\mathcal{L}(g, \theta) = \int_0^1 \mathbb{E}_{\mathbf{x} \sim p(\mathbf{x}), \boldsymbol{\varepsilon} \sim \mathcal{N}(0, \mathbf{I}_n)} \left[\|g(\mathbf{x}_t, t) - (\boldsymbol{\varepsilon} - \mathbf{x})\|^2 \right] \mathrm{d}t \geq \sum_{i=d+1}^{n} \lambda_i \tag{2}$$

where λ_i are the eigenvalues of the covariance matrix of the random variable $W = \boldsymbol{\varepsilon} - \mathbf{x}$.

Notably, when $d \geq n$, $\mathcal{G}_d$ contains the unique minimizer to $\mathcal{L}(\theta)$.

Proof. See Appendix C.1. □

In our toy setting where $p(\mathbf{x}) = \delta(\mathbf{x} - \mathbf{x}_0)$, we have $W \sim \mathcal{N}(-\mathbf{x}, \mathbf{I}_n)$ and $\lambda_i = 1$ for all i. Thus by Theorem 1, the lower bound of the average loss becomes $\tilde{\mathcal{L}}(\theta) \geq \frac{1}{n} \sum_{i=d+1}^{n} 1 = \frac{n-d}{n}$. As shown in Figure 3, this theoretical bound is consistent with our empirical results.

We further extend our investigation to a more practical setting by examining three models of varying width—{DiT-S, DiT-B, DiT-L}. Each model is overfit on a single image encoded by {DINOv2-S, DINOv2-B, DINOv2-L}, respectively, corresponding to different token dimensions. As shown in Section 4.1, convergence occurs only when the model width is at least as large as the token dimension (e.g., DiT-B with DINOv2-B), while the loss fails to converge otherwise (e.g., DiT-S with DINOv2-B).

	DiT-S	DiT-B	DiT-L
DINOv2-S	3.6e−2 ✓	1.0e−3 ✓	9.7e−4 ✓
DINOv2-B	5.2e−1 ✗	2.4e−2 ✓	1.3e−3 ✓
DINOv2-L	6.5e−1 ✗	2.7e−1 ✗	2.2e−2 ✓

Table 3: **Overfitting losses.** Compared between different combinations of model width and token dimension.

- **Suboptimal design for Diffusion Transformers.** *We now fix the width of DiT to be at least as large as the RAE token dimension. For the DINOv2-B RAE, we use DiT-XL in our following experiments.*

4.2 Dimension-Dependent Noise Schedule Shift

Many prior works (Teng et al., 2023; Chen, 2023; Hoogeboom et al., 2023; Esser et al., 2024) have observed that, for inputs $\mathbf{z} \in \mathbb{R}^{C\times H\times W}$, increasing the spatial resolution ($H \times W$) reduces information corruption at the same noise level, impairing diffusion training. These findings, however, are based mainly on pixel- or VAE-encoded inputs with few channels (e.g., $C \leq 16$). In practice, the Gaussian noise is applied to both spatial and channel dimensions; as the number of channels increases, the effective "resolution" per token also grows, reducing information corruption further. We therefore argue that proposed resolution-dependent strategies in these prior works should be generalized to the *effective data dimension*, defined as the number of tokens times their dimensionality.

Concretely, we adopt the shifting strategy of Esser et al. (2024): for a schedule $t_n \in [0, 1]$ and input dimensions n, m, the shifted timestep is defined as $t_m = \frac{\alpha t_n}{1+(\alpha-1)t_n}$ where $\alpha = \sqrt{m/n}$ is a dimension-dependent scaling factor. We follow (Esser et al., 2024) in using $n = 4096$ as the base dimension and set m to the effective data dimension of RAE. As shown in Table 4, this yields significant performance gains, underscoring its importance for training diffusion in the high-dimensional RAE latent space.

	gFID
w/o shift	23.08
w/ shift	4.81

Table 4: **Impact of schedule shift.**

- **Suboptimal noise scheduling.** *We now default the noise schedule to be dimension-dependent for all our following experiments.*

4.3 Noise-Augmented Decoding

Unlike VAEs, where latent tokens are encoded as a continuous distribution $\mathcal{N}(\mu, \sigma^2\mathbf{I})$ (Kingma & Welling, 2014), the RAE decoder D is trained to reconstruct images from the discrete distribution $p(\mathbf{z}) = \sum_i \delta(\mathbf{x} - \mathbf{z}_i)$, where $\mathbf{z}_i$ denotes the training set processed by the RAE encoder E. At inference time, however, the diffusion model may generate latents that are noisy or deviate slightly from the training distribution due to imperfect training and sampling Abuduweili et al. (2024). This creates a significant out-of-distribution challenge for D, hindering sampling quality.

To mitigate this issue, inspired by prior works on Normalizing Flows (Dinh et al., 2017; Ho et al., 2019; Zhai et al., 2025), we augment the RAE decoder training with an additive noise $\mathbf{n} \sim \mathcal{N}(0, \sigma^2\mathbf{I})$. Concretely, rather than decoding directly from the clean latent distribution $p(\mathbf{z})$, we train D on a smoothed distribution $p_{\mathbf{n}}(\mathbf{z}) = \int p(\mathbf{z} - \mathbf{n})\mathcal{N}(0, \sigma^2\mathbf{I})(\mathbf{n})\mathrm{d}\mathbf{n}$ to enhance the decoder's generalization to the denser output space of diffusion models. We further introduce stochasticity into σ by sampling it from $|\mathcal{N}(0, \tau^2)|$, which helps regularize training and improve robustness.

	gFID	rFID
$\mathbf{z} \sim p(\mathbf{z})$	4.81	0.49
$\mathbf{z} \sim p_{\mathbf{n}}(\mathbf{z})$	4.28	0.57

Table 5: **Impact of $p_{\mathbf{n}}(\mathbf{z})$.**

We evaluate impact of $p_{\mathbf{n}}(\mathbf{z})$ on both reconstruction and generation. As shown in Table 5, it improves gFID but slightly worsens rFID. This trade-off is expected: noise smooths the latent distribution and mitigates OOD issues for the decoder, but also removes fine details, reducing reconstruction quality. We conduct more experiments on τ and different encoders in Appendix H.2

- **Diffusion generates noisy latents.** *We now adopt the noise-augmented decoding for all our following experiments.*

Integrating the above techniques, our improved diffusion recipe achieves a gFID of **4.28** (Figure 4) after only 80 epochs and **2.39** after 720 epochs in RAE's latent space. This not only surpasses prior diffusion baselines (Ma et al., 2024) trained on VAE latents (achieving a 47× training speedup), but also matches the convergence speed of recent methods based on representation alignment (Yu et al., 2025), achieving a 16× training speedup. Next, we explore how to further push RAE generation toward state-of-the-art performance.

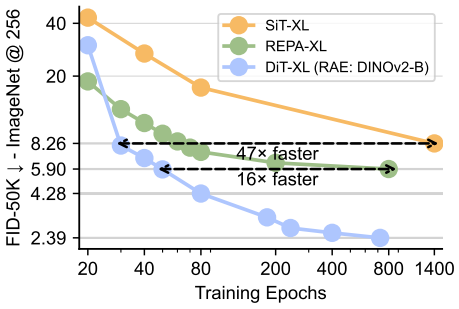

Figure 4: **DiT w/ RAE: faster convergence and better FID.**

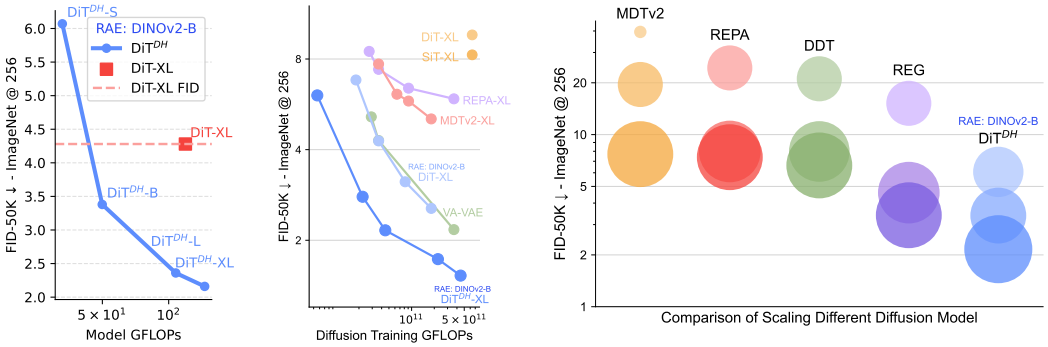

(a) DiT^{DH} scales much better than DiT with RAE

(b) DiT^{DH} with RAE converges faster than VAE-based methods.

(c) DiT^{DH} with RAE reaches better FID than VAE-based methods at all model scales. Bubble area indicates the flops of the model.

Figure 6: **Scalability of DiT^{DH}.** With RAE latents, DiT^{DH} scales more efficiently in both training compute and model size than RAE-based DiT and VAE-based methods.

5 Improving the Model Scalability with Wide Diffusion Head

As discussed in Section 4, within the standard DiT framework, handling higher-dimensional RAE latents requires scaling up the width of the entire backbone, which quickly becomes computationally expensive. To overcome this limitation, we draw inspiration from DDT (Wang et al., 2025c) and introduce the DDT head—a wide, shallow transformer module dedicated to denoising. By attaching this head to a standard DiT, we effectively increase model width without incurring quadratic growth in FLOPs. We refer to this augmented architecture as DiT^{DH} throughout the remainder of the paper. We also conduct experiment of the design choice of DDT head in Appendix H.3

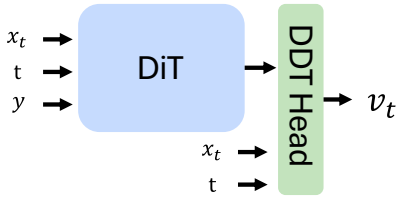

Figure 5: **The Wide DDT Head.**

Wide DDT head. Formally, a DiT^{DH} model consists of a base DiT M and an additional wide, shallow transformer head H. Given a noisy input x_t, timestep t, and an optional class label y, the combined model predicts the velocity v_t as

$$z_t = M(x_t \mid t, y),$$
$$v_t = H(x_t \mid z_t, t),$$

DiT^{DH} converges faster than DiT. We train a series of DiT^{DH} models with varying backbone sizes (DiT^{DH}-S, B, L, and XL) on RAE latents. We use a 2-layer, 2048-dim DDT head for all DiT^{DH} models. Performance is compared against the standard DiT-XL baseline. As shown in Figure 6a, DiT^{DH} is substantially more FLOP-efficient than DiT. For example, DiT^{DH}-B requires only ∼40% of the training FLOPs yet outperforms DiT-XL by a large margin; when scaled to DiT^{DH}-XL under a comparable training budget, DiT^{DH} achieves an FID of 2.16—nearly half that of DiT-XL.

Model	DINOv2		
	S	B	L
DiT-XL	3.50	4.28	6.09
DiT^{DH}-XL	2.42	2.16	2.73

Table 6: **DiT^{DH} outperforms DiT across RAE encoder sizes.**

DiT^{DH} maintains its advantage across RAE scales. We compare DiT^{DH}-XL and DiT-XL on three RAE encoders—DINOv2-S, DINOv2-B, and DINOv2-L. As shown in Section 5, DiT^{DH} consistently outperforms DiT, and the advantage grows with encoder size. For example, with DINOv2-L, DiT^{DH} improves FID from 6.09 to 2.73. We attribute this robustness to the DDT head. Larger encoders produce higher-dimensional latents, which amplify the width bottleneck of DiT. DiT^{DH} addresses this by satisfying the width requirement discussed in Section 4 while keeping features compact. It also filters out noisy information that becomes more prevalent in high-dimensional RAE latents.

Method	Epochs	#Params	Generation@256 w/o guidance				Generation@256 w/ guidance			
			gFID↓	IS↑	Prec.↑	Rec.↑	gFID↓	IS↑	Prec.↑	Rec.↑
Pixel Diffusion										
ADM (Dhariwal & Nichol, 2021)	400	554M	10.94	101.0	0.69	0.63	3.94	215.8	0.83	0.53
RIN (Jabri et al., 2023)	480	410M	3.42	182.0	-	-	-	-	-	-
PixelFlow (Chen et al., 2025e)	320	677M	-	-	-	-	1.98	282.1	0.81	0.60
PixNerd (Wang et al., 2025b)	160	700M	-	-	-	-	2.15	297.0	0.79	0.59
SiD2 (Hoogeboom et al., 2025)	1280	-	-	-	-	-	1.38	-	-	-
Latent Diffusion with VAE										
DiT (Peebles & Xie, 2023)	1400	675M	9.62	121.5	0.67	0.67	2.27	278.2	**0.83**	0.57
MaskDiT (Zheng et al.)	1600	675M	5.69	177.9	0.74	0.60	2.28	276.6	0.80	0.61
SiT (Ma et al., 2024)	1400	675M	8.61	131.7	0.68	0.67	2.06	270.3	0.82	0.59
MDTv2 (Gao et al., 2023)	1080	675M	-	-	-	-	1.58	314.7	0.79	0.65
VA-VAE (Yao et al., 2025)	80	675M	4.29	-	-	-	-	-	-	-
	800		2.17	205.6	0.77	0.65	1.35	295.3	0.79	0.65
REPA (Yu et al., 2025)	80	675M	7.90	122.6	0.70	0.65	-	-	-	-
	800		5.90	157.8	0.70	**0.69**	1.42	305.7	0.80	0.65
DDT (Wang et al., 2025c)	80	675M	6.62	135.2	0.69	0.67	1.52	263.7	0.78	0.63
	400		6.27	154.7	0.68	**0.69**	1.26	310.6	0.79	0.65
REPA-E (Leng et al., 2025)	80	675M	3.46	159.8	0.77	0.63	1.67	266.3	0.80	0.63
	800		1.83	217.3	0.77	0.66	1.26	**314.9**	0.79	0.66
Latent Diffusion with RAE (Ours)										
DiT-XL (DINOv2-S)	800	676M	1.87	209.7	0.80	0.63	1.41	309.41	0.80	0.63
DiT^{DH}-XL (DINOv2-B)	20	839M	3.71	198.7	**0.86**	0.50	–	–	–	–
	80		2.16	214.8	0.82	0.59	–	–	–	–
	800		**1.53**	**238.8**	0.79	0.64	**1.18**	253.42	0.77	**0.67**

Table 7: **Class-conditional performance on ImageNet 256×256.** RAE reaches a gFID of 1.53 at 800 epochs without guidance, outperforming all prior methods by a large margin. It also achieves a state-of-the-art FID of 1.18 with AutoGuidance (details in Appendix D). Besides, RAE surpasses VA-VAE within just 80 training epochs, demonstrating a 10× speedup in convergence.

5.1 State-of-the-Art Diffusion Models

Convergence. We compare the convergence behavior of DiT^{DH}-XL with previous state-of-the-art diffusion models (Peebles & Xie, 2023; Ma et al., 2024; Yu et al., 2025; Gao et al., 2023; Yao et al., 2025) in terms of FID without guidance. In Figure 6b, we show the convergence curve of DiT^{DH}-XL with training epochs/GFLOPs, while baseline models are plotted at their reported final performance. DiT^{DH}-XL already surpasses REPA-XL, MDTv2-XL, and SiT-XL around 5×10^{10} GFLOPs, and by 5×10^{11} GFLOPs it achieves the best FID overall, requiring over 40× less compute.

Scaling. We compare DiT^{DH} with recent methods of different model at different scales. As shown in Figure 6c, increasing the size of DiT^{DH} consistently improves the FID scores. The smallest model, DiT^{DH}-S, reaches a competitive FID of 6.07, already outperforming the much larger REPA-XL. When scaling from DiT^{DH}-S to DiT^{DH}-B, the FID improves significantly from 6.07 to 3.38, surpassing all prior works of similar or even larger scale. The performance continues to improve with DiT^{DH}-XL, setting a new state-of-the-art result of 2.16 at 80 training epochs.

Performance. Finally, we provide a quantitative comparison between DiT^{DH}-XL, our most performant model, with recent state-of-the-art diffusion models on ImageNet 256 × 256 and 512 × 512 in Table 7 and Table 8. Our method outperforms

Method	Generation@512			
	gFID↓	IS↑	Prec.↑	Rec.↑
BigGAN-deep (Brock et al., 2019)	8.43	177.9	**0.88**	0.29
StyleGAN-XL (Sauer et al., 2022)	2.41	267.8	0.77	0.52
VAR (Tian et al., 2024)	2.63	303.2	-	-
MAGVIT-v2 (Yu et al., 2024a)	1.91	**324.3**	-	-
XAR (Ren et al., 2025)	1.70	281.5	-	-
ADM	3.85	221.7	0.84	0.53
SiD2	1.50	-	-	-
DiT	3.04	240.8	0.84	0.54
SiT	2.62	252.2	0.84	0.57
DiffiT (Hatamizadeh et al., 2024)	2.67	252.1	0.83	0.55
REPA	2.08	274.6	0.83	0.58
DDT	1.28	305.1	0.80	**0.63**
EDM2 (Karras et al., 2024)	1.25	-	-	-
DiT^{DH}-XL (DINOv2-B)	**1.13**	259.6	0.80	**0.63**

Table 8: **Class-conditional performance on ImageNet 512×512.** Baseline methods are reported with guidance. DiT^{DH} with guidance achieves a new state-of-the-art FID score of 1.13.

all prior diffusion models by a large margin, setting new state-of-the-art FID scores of **1.53** without guidance and **1.18** with guidance at 256×256. On 512×512, DiT^{DH}-XL further achieves a new state-of-the-art FID of **1.13** with guidance, surpassing the previous best performance achieved by EDM2 (1.25) within 400 training epochs. We provide visualization samples in Appendix L and unconditional generation results in Appendix K.

6 Discussions

6.1 How can RAE extend to high-resolution synthesis efficiently?

A central challenge in generating high-resolution images is that resolution scales with the number of tokens: doubling image size in each dimension requires roughly four times as many tokens. To address this, we propose to shift the resolution burden to the decoder. Specifically, we allow the decoder patch size p_d to differ from the encoder patch size p_e. When $p_d = p_e$, the output matches the input resolution; setting $p_d = 2p_e$ upsamples by $2\times$ per dimension, reconstructing a 512×512 image from the same tokens used at 256×256.

Since the decoder is decoupled from both the encoder and the diffusion process, we can reuse diffusion models trained at 256×256 resolution, simply swapping in an upsampling decoder to produce 512×512 outputs without retraining. As shown in Table 9, this approach slightly increases rFID but achieves competitive gFID compared to VAE-based methods, while being $4\times$ more efficient than quadrupling the number of tokens.

Method	#Tokens	gFID ↓	rFID↓
Direct	1024	1.13	0.53
Upsample	256	1.61	0.97

Table 9: **Comparison on ImageNet 512×512.** Direct: directly increasing tokens; Upsamling: use decoder upsamling. Both models are trained for 400 epochs.

6.2 Does DiT^{DH} work without RAE?

In this work, we propose and study RAE and DiT^{DH}. In Section 4, we showed that RAE with DiT already brings substantial benefits, even without DiT^{DH}. Here, we ask the reverse question: can DiT^{DH} still provide improvements, without the latent space of RAE?

	VAE	DINOv2-B
DiT-XL	7.13	4.28
DiT^{DH}-XL	11.70	2.16

Table 10: **Performance on VAE.** DiT^{DH} yields worse FID than DiT, despite using extra compute.

To investigate, we train both DiT-XL and DiT^{DH}-XL on SD-VAE latents with a patch size of 2, alongside DINOv2-B for comparison, for 80 epochs, and report unguided FID. As shown in Table 10, DiT^{DH}-XL performs even worse than DiT-XL on SD-VAE, despite the additional computation introduced by the diffusion head. This indicates that the DDT head provides little benefit in low-dimensional latent spaces, and its primary strength arises in high-dimensional diffusion tasks introduced by RAE.

6.3 How important is structured representation in high-dimensional diffusion?

DiT^{DH} achieves strong performance when paired with the high-dimensional latent space of RAE. This raises a key question: is the structured representation of RAE essential, or would DiT^{DH} work equally well on unstructured high-dimensional inputs such as raw pixels?

To test this, we train DiT-XL and DiT^{DH}-XL directly on pixels, matching the dimensionality of DINOv2-B latents with a patch size of 16, and report unguided FID at 80 epochs. As shown in Table 11, DiT^{DH} does significantly improve over DiT on pixels, but both models perform far worse than their counterparts trained on RAE latents. These results demonstrate that high dimensionality alone is not sufficient: the structured representation provided by RAE is what makes the gains truly substantial.

	Pixel	DINOv2-B
DiT-XL	51.09	4.28
DiT^{DH}-XL	30.56	2.16

Table 11: **Comparison on pixel diffusion.** Pixel Diffusion has much worse FID than diffusion on DINOv2-B.

REFERENCES

Abulikemu Abuduweili, Chenyang Yuan, Changliu Liu, and Frank Permenter. Enhancing sample generation of diffusion models using noise level correction. *TMLR*, 2024. 6

Michael S Albergo, Nicholas M Boffi, and Eric Vanden-Eijnden. Stochastic interpolants: A unifying framework for flows and diffusions. *arXiv preprint arXiv:2303.08797*, 2023. 17, 23

Andrew Brock, Jeff Donahue, and Karen Simonyan. Large scale gan training for high fidelity natural image synthesis. In *ICLR*, 2019. 8

Shiyue Cao, Yueqin Yin, Lianghua Huang, Yu Liu, Xin Zhao, Deli Zhao, and Kaigi Huang. Efficient-vqgan: Towards high-resolution image generation with efficient vision transformers. In *ICCV*, 2023. 16

Mathilde Caron, Hugo Touvron, Ishan Misra, Hervé Jégou, Julien Mairal, Piotr Bojanowski, and Armand Joulin. Emerging properties in self-supervised vision transformers. In *ICCV*, 2021a. 2

Mathilde Caron, Hugo Touvron, Ishan Misra, Hervé Jégou, Julien Mairal, Piotr Bojanowski, and Armand Joulin. Emerging properties in self-supervised vision transformers. In *ICCV*, 2021b. 20

Hao Chen, Yujin Han, Fangyi Chen, Xiang Li, Yidong Wang, Jindong Wang, Ze Wang, Zicheng Liu, Difan Zou, and Bhiksha Raj. Masked autoencoders are effective tokenizers for diffusion models. In *ICML*, 2025a. 2, 3

Jiuhai Chen, Zhiyang Xu, Xichen Pan, Yushi Hu, Can Qin, Tom Goldstein, Lifu Huang, Tianyi Zhou, Saining Xie, Silvio Savarese, Le Xue, Caiming Xiong, and Ran Xu. Blip3-o: A family of fully open unified multimodal models-architecture, training and dataset, 2025b. 16

Junyu Chen, Han Cai, Junsong Chen, Enze Xie, Shang Yang, Haotian Tang, Muyang Li, Yao Lu, and Song Han. Deep compression autoencoder for efficient high-resolution diffusion models. In *ICLR*, 2025c. 16

Junyu Chen, Dongyun Zou, Wenkun He, Junsong Chen, Enze Xie, Song Han, and Han Cai. Dc-ae 1.5: Accelerating diffusion model convergence with structured latent space, 2025d. 2, 3

Mark Chen, Alec Radford, Rewon Child, Jeffrey Wu, Heewoo Jun, David Luan, and Ilya Sutskever. Generative pretraining from pixels. In *ICML*, 2020. 16

Shoufa Chen, Chongjian Ge, Shilong Zhang, Peize Sun, and Ping Luo. Pixelflow: Pixel-space generative models with flow. *arXiv preprint arXiv:2504.07963*, 2025e. 8

Ting Chen. On the importance of noise scheduling for diffusion models. *arXiv preprint arXiv:2301.10972*, 2023. 2, 6

Timothée Darcet, Maxime Oquab, Julien Mairal, and Piotr Bojanowski. Vision transformers need registers. In *ICLR*, 2025. 19

Prafulla Dhariwal and Alexander Nichol. Diffusion models beat GANs on image synthesis. In *NeurIPS*, 2021. 8, 23

Laurent Dinh, Jascha Sohl-Dickstein, and Samy Bengio. Density estimation using real nvp. In *ICLR*, 2017. 6

Alexey Dosovitskiy, Lucas Beyer, Alexander Kolesnikov, Dirk Weissenborn, Xiaohua Zhai, Thomas Unterthiner, Mostafa Dehghani, Matthias Minderer, Georg Heigold, Sylvain Gelly, et al. An image is worth 16x16 words: Transformers for image recognition at scale. In *ICLR*, 2021. 16, 19

Patrick Esser, Robin Rombach, and Björn Ommer. Taming transformers for high-resolution image synthesis. In *CVPR*, 2021. 3, 16, 20

Patrick Esser, Sumith Kulal, Andreas Blattmann, Rahim Entezari, Jonas Müller, Harry Saini, Yam Levi, Dominik Lorenz, Axel Sauer, Frederic Boesel, Dustin Podell, Tim Dockhorn, Zion English, Kyle Lacey, Alex Goodwin, Yannik Marek, and Robin Rombach. Scaling rectified flow transformers for high-resolution image synthesis. In *ICML*, 2024. 1, 2, 6, 23

David Fan, Shengbang Tong, Jiachen Zhu, Koustuv Sinha, Zhuang Liu, Xinlei Chen, Michael Rabbat, Nicolas Ballas, Yann LeCun, Amir Bar, et al. Scaling language-free visual representation learning. In *ICCV*, 2025a. 28, 29

Lijie Fan, Tianhong Li, Siyang Qin, Yuanzhen Li, Chen Sun, Michael Rubinstein, Deqing Sun, Kaiming He, and Yonglong Tian. Fluid: Scaling autoregressive text-to-image generative models with continuous tokens. In *ICLR*, 2025b. 16

Shanghua Gao, Pan Zhou, Ming-Ming Cheng, and Shuicheng Yan. Mdtv2: Masked diffusion transformer is a strong image synthesizer. *arXiv preprint arXiv:2303.14389*, 2023. 8

Ian Goodfellow, Jean Pouget-Abadie, Mehdi Mirza, Bing Xu, David Warde-Farley, Sherjil Ozair, Aaron Courville, and Yoshua Bengio. Generative adversarial nets. In *NeurIPS*, 2014. 3

Philippe Hansen-Estruch, David Yan, Ching-Yao Chung, Orr Zohar, Jialiang Wang, Tingbo Hou, Tao Xu, Sriram Vishwanath, Peter Vajda, and Xinlei Chen. Learnings from scaling visual tokenizers for reconstruction and generation. In *ICML*, 2025. 16

Ali Hatamizadeh, Jiaming Song, Guilin Liu, Jan Kautz, and Arash Vahdat. DiffiT: Diffusion vision transformers for image generation. In *ECCV*, 2024. 8

Kaiming He, Xinlei Chen, Saining Xie, Yanghao Li, Piotr Dollár, and Ross Girshick. Masked autoencoders are scalable vision learners. In *CVPR*, 2021. 2, 3, 20

Martin Heusel, Hubert Ramsauer, Thomas Unterthiner, Bernhard Nessler, and Sepp Hochreiter. GANs trained by a two time-scale update rule converge to a local nash equilibrium. In *NeurIPS*, 2017. 4, 24

Geoffrey E Hinton and Ruslan R Salakhutdinov. Reducing the dimensionality of data with neural networks. *science*, 313(5786), 2006. 16

Jonathan Ho and Tim Salimans. Classifier-free diffusion guidance, 2022. 19

Jonathan Ho, Xi Chen, Aravind Srinivas, Yan Duan, and Pieter Abbeel. Flow++: Improving flow-based generative models with variational dequantization and architecture design. In *ICML*, 2019. 6

Jonathan Ho, Ajay Jain, and Pieter Abbeel. Denoising diffusion probabilistic models. In *NeurIPS*, 2020. 16, 23

Emiel Hoogeboom, Jonathan Heek, and Tim Salimans. Simple diffusion: End-to-end diffusion for high resolution images. In *ICML*, 2023. 2, 6

Emiel Hoogeboom, Thomas Mensink, Jonathan Heek, Kay Lamerigts, Ruiqi Gao, and Tim Salimans. Simpler diffusion (sid2): 1.5 fid on imagenet512 with pixel-space diffusion. In *CVPR*, 2025. 8

Allan Jabri, David Fleet, and Ting Chen. Scalable adaptive computation for iterative generation. In *ICML*, 2023. 8

Tero Karras, Miika Aittala, Timo Aila, and Samuli Laine. Elucidating the design space of diffusion-based generative models. In *NeurIPS*, 2022. 23

Tero Karras, Miika Aittala, Jaakko Lehtinen, Janne Hellsten, Timo Aila, and Samuli Laine. Analyzing and improving the training dynamics of diffusion models. In *CVPR*, 2024. 8

Tero Karras, Miika Aittala, Tuomas Kynkäänniemi, Jaakko Lehtinen, Timo Aila, and Samuli Laine. Guiding a diffusion model with a bad version of itself. In *NeurIPS*, 2025. 2, 19

Diederik P Kingma and Max Welling. Auto-encoding variational bayes. In *ICLR*, 2014. 1, 2, 3, 6, 16

Theodoros Kouzelis, Ioannis Kakogeorgiou, Spyros Gidaris, and Nikos Komodakis. Eq-vae: Equivariance regularized latent space for improved generative image modeling. In *ICML*, 2025a. 16

Theodoros Kouzelis, Efstathios Karypidis, Ioannis Kakogeorgiou, Spyros Gidaris, and Nikos Komodakis. Boosting generative image modeling via joint image-feature synthesis. In *NeurIPS*, 2025b. 3

Tuomas Kynkäänniemi, Tero Karras, Samuli Laine, Jaakko Lehtinen, and Timo Aila. Improved precision and recall metric for assessing generative models. In *NeurIPS*, 2019. 24

Tuomas Kynkäänniemi, Miika Aittala, Tero Karras, Samuli Laine, Timo Aila, and Jaakko Lehtinen. Applying guidance in a limited interval improves sample and distribution quality in diffusion models. In *NeurIPS*, 2024. 19

Black Forest Labs. Flux. https://github.com/black-forest-labs/flux, 2024. 1, 29

Doyup Lee, Chiheon Kim, Saehoon Kim, Minsu Cho, and Wook-Shin Han. Autoregressive image generation using residual quantization. In *CVPR*, 2022. 16

Xingjian Leng, Jaskirat Singh, Yunzhong Hou, Zhenchang Xing, Saining Xie, and Liang Zheng. Repa-e: Unlocking vae for end-to-end tuning with latent diffusion transformers. In *ICCV*, 2025. 8

Tianhong Li, Dina Katabi, and Kaiming He. Return of unconditional generation: A self-supervised representation generation method. In *NeurIPS*, 2024a. 24

Tianhong Li, Yonglong Tian, He Li, Mingyang Deng, and Kaiming He. Autoregressive image generation without vector quantization. In *NeurIPS*, 2024b. 16

Yaron Lipman, Ricky TQ Chen, Heli Ben-Hamu, Maximilian Nickel, and Matt Le. Flow matching for generative modeling. In *ICLR*, 2023. 4, 23

Bingchen Liu, Ehsan Akhgari, Alexander Visheratin, Aleks Kamko, Linmiao Xu, Shivam Shrirao, Chase Lambert, Joao Souza, Suhail Doshi, and Daiqing Li. Playground v3: Improving text-to-image alignment with deep-fusion large language models, 2024. 1

Xingchao Liu, Chengyue Gong, and Qiang Liu. Flow straight and fast: Learning to generate and transfer data with rectified flow. In *ICLR*, 2023. 4, 23

Nanye Ma, Mark Goldstein, Michael S Albergo, Nicholas M Boffi, Eric Vanden-Eijnden, and Saining Xie. Sit: Exploring flow and diffusion-based generative models with scalable interpolant transformers. In *ECCV*, 2024. 2, 3, 6, 8, 16, 23, 28

Fabian Mentzer, David Minnen, Eirikur Agustsson, and Michael Tschannen. Finite scalar quantization: VQ-VAE made simple. In *ICLR*, 2024. 16

Alex Nichol and Prafulla Dhariwal. Improved denoising diffusion probabilistic models. In *ICML*, 2021. 16

Aaron van den Oord, Oriol Vinyals, and Koray Kavukcuoglu. Neural discrete representation learning. In *NeurIPS*, 2017. 16

Maxime Oquab, Timothée Darcet, Théo Moutakanni, Huy Vo, Marc Szafraniec, Vasil Khalidov, Pierre Fernandez, Daniel Haziza, Francisco Massa, Alaaeldin El-Nouby, et al. Dinov2: Learning robust visual features without supervision. *TMLR*, 2023. 3

Xichen Pan, Satya Narayan Shukla, Aashu Singh, Zhuokai Zhao, Shlok Kumar Mishra, Jialiang Wang, Zhiyang Xu, Jiuhai Chen, Kunpeng Li, Felix Juefei-Xu, Ji Hou, and Saining Xie. Transfer between modalities with metaqueries, 2025. 1, 16, 29

Niki Parmar, Ashish Vaswani, Jakob Uszkoreit, Lukasz Kaiser, Noam Shazeer, Alexander Ku, and Dustin Tran. Image transformer. In *ICML*, 2018. 16

William Peebles and Saining Xie. Scalable diffusion models with transformers. In *ICCV*, 2023. 1, 2, 3, 4, 8, 16

Kai Qiu, Xiang Li, Hao Chen, Jason Kuen, Xiaohao Xu, Jiuxiang Gu, Yinyi Luo, Bhiksha Raj, Zhe Lin, and Marios Savvides. Image tokenizer needs post-training, 2025. URL https://arxiv.org/abs/2509.12474. 16

Vivek Ramanujan, Kushal Tirumala, Armen Aghajanyan, Luke Zettlemoyer, and Ali Farhadi. When worse is better: Navigating the compression-generation tradeoff in visual tokenization. In *NeurIPS*, 2025. 16

Aditya Ramesh, Prafulla Dhariwal, Alex Nichol, Casey Chu, and Mark Chen. Hierarchical text-conditional image generation with clip latents. *arXiv preprint arXiv:2204.06125*, 1(2):3, 2022. 16

Ali Razavi, Aaron van den Oord, and Oriol Vinyals. Generating diverse high-fidelity images with vq-vae-2. In *NeurIPS*, 2019. 16

Sucheng Ren, Qihang Yu, Ju He, Xiaohui Shen, Alan Yuille, and Liang-Chieh Chen. Beyond next-token: Next-x prediction for autoregressive visual generation. *arXiv preprint arXiv:2502.20388*, 2025. 8

Robin Rombach, Andreas Blattmann, Dominik Lorenz, Patrick Esser, and Björn Ommer. High-resolution image synthesis with latent diffusion models. In *CVPR*, 2022. 1, 3, 16

Olga Russakovsky, Jia Deng, Hao Su, Jonathan Krause, Sanjeev Satheesh, Sean Ma, Zhiheng Huang, Andrej Karpathy, Aditya Khosla, Michael Bernstein, et al. Imagenet large scale visual recognition challenge. *International journal of computer vision*, 115(3):211–252, 2015. 3

Tim Salimans, Ian Goodfellow, Wojciech Zaremba, Vicki Cheung, Alec Radford, and Xi Chen. Improved techniques for training GANs. In *NeurIPS*, 2016. 24

Axel Sauer, Katja Schwarz, and Andreas Geiger. Stylegan-xl: Scaling stylegan to large diverse datasets. In *SIGGRAPH*, 2022. 8

Axel Sauer, Tero Karras, Samuli Laine, Andreas Geiger, and Timo Aila. Stylegan-t: Unlocking the power of gans for fast large-scale text-to-image synthesis. In *ICML*, 2023. 20

Ivan Skorokhodov, Sharath Girish, Benran Hu, Willi Menapace, Yanyu Li, Rameen Abdal, Sergey Tulyakov, and Aliaksandr Siarohin. Improving the diffusability of autoencoders. In *ICML*, 2025. 4

Yang Song, Jascha Sohl-Dickstein, Diederik P. Kingma, Abhishek Kumar, Stefano Ermon, and Ben Poole. Score-based generative modeling through stochastic differential equations. In *ICLR*, 2021. 21

Quan Sun, Yufeng Cui, Xiaosong Zhang, Fan Zhang, Qiying Yu, Zhengxiong Luo, Yueze Wang, Yongming Rao, Jingjing Liu, Tiejun Huang, and Xinlong Wang. Generative multimodal models are in-context learners. In *CVPR*, 2024. 16

Christian Szegedy, Vincent Vanhoucke, Sergey Ioffe, Jon Shlens, and Zbigniew Wojna. Rethinking the Inception architecture for computer vision. In *CVPR*, 2016. 24

Bingda Tang, Boyang Zheng, Sayak Paul, and Saining Xie. Exploring the deep fusion of large language models and diffusion transformers for text-to-image synthesis. In *Proceedings of the Computer Vision and Pattern Recognition Conference*, pp. 28586–28595, 2025a. 29

Hao Tang, Chenwei Xie, Xiaoyi Bao, Tingyu Weng, Pandeng Li, Yun Zheng, and Liwei Wang. Unilip: Adapting clip for unified multimodal understanding, generation and editing, 2025b. 3, 16

Jiayan Teng, Wendi Zheng, Ming Ding, Wenyi Hong, Jianqiao Wangni, Zhuoyi Yang, and Jie Tang. Relay diffusion: Unifying diffusion process across resolutions for image synthesis. In *ICLR*, 2023. 6

Bart Thomee, David A Shamma, Gerald Friedland, Benjamin Elizalde, Karl Ni, Douglas Poland, Damian Borth, and Li-Jia Li. Yfcc100m: The new data in multimedia research. *Communications of the ACM*, 59(2):64–73, 2016. 28

Keyu Tian, Yi Jiang, Zehuan Yuan, Bingyue Peng, and Liwei Wang. Visual autoregressive modeling: Scalable image generation via next-scale prediction. In *NeurIPS*, 2024. 8

Shengbang Tong, Ellis Brown, Penghao Wu, Sanghyun Woo, Manoj Middepogu, Sai Charitha Akula, Jihan Yang, Shusheng Yang, Adithya Iyer, Xichen Pan, et al. Cambrian-1: A fully open, vision-centric exploration of multimodal llms. In *NeurIPS*, 2024. 29

Shengbang Tong, David Fan, Jiachen Zhu, Yunyang Xiong, Xinlei Chen, Koustuv Sinha, Michael Rabbat, Yann LeCun, Saining Xie, and Zhuang Liu. Metamorph: Multimodal understanding and generation via instruction tuning. In *ICCV*, 2025. 1, 16

Michael Tschannen, Alexey Gritsenko, Xiao Wang, Muhammad Ferjad Naeem, Ibrahim Alabdulmohsin, Nikhil Parthasarathy, Talfan Evans, Lucas Beyer, Ye Xia, Basil Mustafa, Olivier Hénaff, Jeremiah Harmsen, Andreas Steiner, and Xiaohua Zhai. Siglip 2: Multilingual vision-language encoders with improved semantic understanding, localization, and dense features, 2025. 2, 3, 28

Pascal Vincent, Hugo Larochelle, Yoshua Bengio, and Pierre-Antoine Manzagol. Extracting and composing robust features with denoising autoencoders. In *ICML*, 2008. 3, 16

Hanyu Wang, Saksham Suri, Yixuan Ren, Hao Chen, and Abhinav Shrivastava. Larp: Tokenizing videos with a learned autoregressive generative prior. In *ICLR*, 2025a. 16

Shuai Wang, Ziteng Gao, Chenhui Zhu, Weilin Huang, and Limin Wang. Pixnerd: Pixel neural field diffusion. *arXiv preprint arXiv:2507.23268*, 2025b. 8

Shuai Wang, Zhi Tian, Weilin Huang, and Limin Wang. Ddt: Decoupled diffusion transformer, 2025c. 2, 3, 7, 8, 28

Ge Wu, Shen Zhang, Ruijing Shi, Shanghua Gao, Zhenyuan Chen, Lei Wang, Zhaowei Chen, Hongcheng Gao, Yao Tang, Jian Yang, Ming-Ming Cheng, and Xiang Li. Representation entanglement for generation:training diffusion transformers is much easier than you think, 2025. 3

Jiawei Yang, Tianhong Li, Lijie Fan, Yonglong Tian, and Yue Wang. Latent denoising makes good visual tokenizers, 2025. 2, 3, 16, 17

Jingfeng Yao, Bin Yang, and Xinggang Wang. Reconstruction vs. generation: Taming optimization dilemma in latent diffusion models. In *CVPR*, 2025. 1, 2, 3, 4, 8, 21

Jiahui Yu, Yuanzhong Xu, Jing Yu Koh, Thang Luong, Gunjan Baid, Zirui Wang, Vijay Vasudevan, Alexander Ku, Yinfei Yang, Burcu Karagol Ayan, et al. Scaling autoregressive models for content-rich text-to-image generation. *TMLR*, 2022. 16

Lijun Yu, José Lezama, Nitesh B Gundavarapu, Luca Versari, Kihyuk Sohn, David Minnen, Yong Cheng, Vighnesh Birodkar, Agrim Gupta, Xiuye Gu, et al. Language model beats diffusion–tokenizer is key to visual generation. In *ICLR*, 2024a. 8

Qihang Yu, Mark Weber, Xueqing Deng, Xiaohui Shen, Daniel Cremers, and Liang-Chieh Chen. An image is worth 32 tokens for reconstruction and generation. In *NeurIPS*, 2024b. 3, 16

Sihyun Yu, Sangkyung Kwak, Huiwon Jang, Jongheon Jeong, Jonathan Huang, Jinwoo Shin, and Saining Xie. Representation alignment for generation: Training diffusion transformers is easier than you think. In *ICLR*, 2025. 2, 3, 6, 8, 16, 28

Shuangfei Zhai, Ruixiang Zhang, Preetum Nakkiran, David Berthelot, Jiatao Gu, Huangjie Zheng, Tianrong Chen, Miguel Angel Bautista, Navdeep Jaitly, and Josh Susskind. Normalizing flows are capable generative models. In *ICML*, 2025. 6

Richard Zhang, Phillip Isola, Alexei A. Efros, Eli Shechtman, and Oliver Wang. The unreasonable effectiveness of deep features as a perceptual metric. In *CVPR*, 2018. 3

Shengyu Zhao, Zhijian Liu, Ji Lin, Jun-Yan Zhu, and Song Han. Differentiable augmentation for data-efficient gan training. In *NeurIPS*, 2020. 20

Yue Zhao, Yuanjun Xiong, and Philipp Krähenbühl. Image and video tokenization with binary spherical quantization. In *ICLR*, 2025. 16

Anlin Zheng, Xin Wen, Xuanyang Zhang, Chuofan Ma, Tiancai Wang, Gang Yu, Xiangyu Zhang, and Xiaojuan Qi. Vision foundation models as effective visual tokenizers for autoregressive image generation, 2025. 16

Chuanxia Zheng, Tung-Long Vuong, Jianfei Cai, and Dinh Phung. Movq: Modulating quantized vectors for high-fidelity image generation. In *NeurIPS*, 2022. 16

Hongkai Zheng, Weili Nie, Arash Vahdat, and Anima Anandkumar. Fast training of diffusion models with masked transformers. *TMLR*. 8

Jinguo Zhu, Weiyun Wang, Zhe Chen, Zhaoyang Liu, Shenglong Ye, Lixin Gu, Hao Tian, Yuchen Duan, Weijie Su, Jie Shao, Zhangwei Gao, Erfei Cui, Xuehui Wang, Yue Cao, Yangzhou Liu, Xingguang Wei, Hongjie Zhang, Haomin Wang, Weiye Xu, Hao Li, Jiahao Wang, Nianchen Deng, Songze Li, Yinan He, Tan Jiang, Jiapeng Luo, Yi Wang, Conghui He, Botian Shi, Xingcheng Zhang, Wenqi Shao, Junjun He, Yingtong Xiong, Wenwen Qu, Peng Sun, Penglong Jiao, Han Lv, Lijun Wu, Kaipeng Zhang, Huipeng Deng, Jiaye Ge, Kai Chen, Limin Wang, Min Dou, Lewei Lu, Xizhou Zhu, Tong Lu, Dahua Lin, Yu Qiao, Jifeng Dai, and Wenhai Wang. Internvl3: Exploring advanced training and test-time recipes for open-source multimodal models, 2025. 16

Yongxin Zhu, Bocheng Li, Hang Zhang, Xin Li, Linli Xu, and Lidong Bing. Stabilize the latent space for image autoregressive modeling: A unified perspective. In *NeurIPS*, 2024. 16

A LLM USE CLAIM

We utilized a large language model (LLM) to assist in the writing and editing process of this manuscript. The LLM was primarily used for improving grammar, clarity, and readability. This included tasks such as rephrasing sentences, correcting spelling and grammatical errors, and ensuring consistent style throughout the paper. All authors have reviewed and edited the final version of the manuscript and take full responsibility for its content.

B EXTENDED RELATED WORK

Representation encoder as autoencoder. Recent studies have investigated leveraging semantic representations for reconstruction, particularly in MLLMs where diffusion decoders are conditioned on semantic tokens (Sun et al., 2024; Chen et al., 2025b; Pan et al., 2025; Tong et al., 2025). While this improves visual quality, the reliance on large pretrained diffusion decoders makes reconstructions less faithful to the input, limiting their effectiveness as true autoencoders. Very recently, UniLIP (Tang et al., 2025b) employs a one-step convolutional decoder on top of InternViT (Zhu et al., 2025), achieving reconstruction quality surpassing SD-VAE. However, UniLIP relies on additional large-scale fine-tuning of pretrained ViTs, arguing that frozen pretrained representation encoders lacks sufficient visual detail. In contrast, we show this is not the case: frozen representation encoders achieves comparable reconstruction performance while enabling much faster convergence in diffusion training.

Another line of related work also try to utilize representation encoders directly as tokenizers. VFMTok (Zheng et al., 2025) and DiGIT (Zhu et al., 2024) applies vector-quantization directly to pretrained representation encoders like Dino or SigLIP. These approaches transform representation encoders into an effective tokenizer for AR models, but still suffer from the information capacity bottleneck brought by quantization.

Compressed Image Tokenizers. Autoencoders have long been used to compress images into low-dimensional representations for reconstruction (Hinton & Salakhutdinov, 2006; Vincent et al., 2008). VAEs (Kingma & Welling, 2014) extend this paradigm by mapping inputs to Gaussian distributions, while VQ-VAEs (Oord et al., 2017; Razavi et al., 2019) introduce discrete latent codes. VQGAN (Esser et al., 2021) adds adversarial objectives, and ViT-VQGAN (Esser et al., 2021; Cao et al., 2023) modernizes the architecture with Vision Transformers (ViTs) (Dosovitskiy et al., 2021). Other advances include multi-stage quantization (Lee et al., 2022; Zheng et al., 2022), lookup-free schemes (Mentzer et al., 2024; Zhao et al., 2025), token-efficient designs such as TiTok and DCAE (Yu et al., 2024b; Chen et al., 2025c), and structure-preserving approaches like EQVAE (Kouzelis et al., 2025a). (Hansen-Estruch et al., 2025) further explores the scaling behavior of VAEs. LARP, CRT, REPA-E (Wang et al., 2025a; Ramanujan et al., 2025; Yu et al., 2025) tried to improve VAE with generative priors via back-propagation. In contrast, we dispense with aggressive compression and instead adopt a pretrained representation encoders as encoder. This avoids the encoder collapsing into shallow features optimized only for reconstruction loss, while providing strong pretrained representations that serve as a robust latent space.

Generative Models. Modern image generation is dominated by two paradigms: autoregressive (AR) models and diffusion models. AR models (Ramesh et al., 2022; Yu et al., 2022; Parmar et al., 2018; Chen et al., 2020) generate images sequentially, token by token, and benefit from powerful language-model architectures but often suffer from slow sampling. Diffusion models (Ho et al., 2020; Nichol & Dhariwal, 2021; Rombach et al., 2022; Ma et al., 2024; Peebles & Xie, 2023) instead learn to iteratively denoise noisy signals, offering superior sample quality and scalability, though at the cost of many sampling steps. In this work, we build on diffusion models but adapt them to high-dimensional latent spaces provided by pretrained representation encoders. We find representation encoders provide faster convergence and improved scaling behavior.

Robust decoders for generation. Recent works suggest that incorporating masking or latent denoising losses can improve tokenizer training. *l*-DeTok (Yang et al., 2025) shows that combining both losses yields strong VAEs for second-stage MAR (Li et al., 2024b; Fan et al., 2025b) generation, while RobusTok (Qiu et al., 2025) demonstrates that training with perturbed tokens makes decoders

more robust. Notably, Yang et al. (2025) report that denoising loss only increase performance when encoder and decoder are jointly trained, whereas we observe substantial gains in generation quality with frozen encoders.

C PROOFS

C.1 PROOF OF LOWER BOUND FOR TRAINING LOSS

Theorem 1. *Assuming $\mathbf{x} \sim p(\mathbf{x}) \in \mathbb{R}^n, \boldsymbol{\varepsilon} \sim \mathcal{N}(0, \mathbf{I}_n)$, $t \in [0,1]$. Let $\mathbf{x}_t = (1-t)\mathbf{x} + t\boldsymbol{\varepsilon}$, consider the function family*

$$\mathcal{G}_d = \{g(\mathbf{x}_t, t) = \boldsymbol{B} f(\boldsymbol{A}\mathbf{x}_t, t) : \boldsymbol{A} \in \mathbb{R}^{d\times n}, \boldsymbol{B} \in \mathbb{R}^{n\times d}, f : [0,1] \times \mathbb{R}^d \to \mathbb{R}^d\} \tag{1}$$

*where $d < n$, f refers to a stack of standard DiT blocks whose width is smaller than the token dimension from the representation encoder, and $\boldsymbol{A}, \boldsymbol{B}$ denote the input and output linear projections, respectively. Then for **any** $g \in \mathcal{G}_d$,*

$$\mathcal{L}(g, \theta) = \int_0^1 \mathbb{E}_{\mathbf{x}\sim p(\mathbf{x}), \boldsymbol{\varepsilon}\sim\mathcal{N}(0,\mathbf{I}_n)} \left[\|g(\mathbf{x}_t, t) - (\boldsymbol{\varepsilon} - \mathbf{x})\|^2\right] \mathrm{d}t \geq \sum_{i=d+1}^{n} \lambda_i \tag{2}$$

where λ_i are the eigenvalues of the covariance matrix of the random variable $W = \boldsymbol{\varepsilon} - \mathbf{x}$.

Notably, when $d \geq n$, $\mathcal{G}_d$ contains the unique minimizer to $\mathcal{L}(\theta)$.

Proof. By Albergo et al. (2023), the distribution ρ_t of $\mathbf{x}_t$ satisfies $\rho_0 = p(\mathbf{x})$, $\rho_1 = \mathcal{N}(0, \mathbf{I}_n)$, and $\partial_t \rho + \nabla \cdot (v\rho) = 0$ where v is the optimal velocity predictor defined as $v(\mathbf{x}_t, t) = \mathbb{E}[\boldsymbol{\varepsilon} - \mathbf{x} | \mathbf{x}_t]$. Also, by Theorem 2.7 in Albergo et al. (2023), there exists $f^* \in C^0((C^1(\mathbb{R}^n))^n; [0,1])$[1] that uniquely minimizes the $\mathcal{L}(f, \theta)$ and perfectly approximates v.

By our training setting, it's reasonable to assume that $\mathbf{x} \sim p(\mathbf{x})$ and $\boldsymbol{\varepsilon} \sim \mathcal{N}(0, \mathbf{I}_n)$ are independent. Then the distribution of the objective $\mathbf{y} = \boldsymbol{\varepsilon} - \mathbf{x} \sim p_{\mathbf{y}}(\mathbf{y})$ satisfies $p_{\mathbf{y}}(\mathbf{y}) = \int_{\mathbb{R}^n} \mathcal{N}(0, \mathbf{I}_n)(\mathbf{y} + \mathbf{x}) p(\mathbf{x}) \mathrm{d}\mathbf{x}$. Clearly, $p_{\mathbf{y}}$ has full support on $\mathbb{R}^n$ and is strictly positive, indicating $\mathbf{y}$ has a non-zero probability anywhere in $\mathbb{R}^n$. Similarly, for $\mathbf{x}_t = (1-t)\mathbf{x} + t\boldsymbol{\varepsilon}$, given any t, $p_{\mathbf{x}_t}(\mathbf{w}) = \int_{\mathbb{R}^n} \mathcal{N}(0, t^2\mathbf{I}_n)(\mathbf{w} - \mathbf{x}) \frac{1}{(1-t)} p(\frac{\mathbf{x}}{1-t}) \mathrm{d}\mathbf{x}$ also has full support on $\mathbb{R}^n$ and is strictly positive, indicating $\mathbf{x}_t$ has a non-zero probability anywhere in $\mathbb{R}^n$ as well.

Recall that for any function $f : \mathcal{X} \to \mathcal{Y}$, $\mathrm{Im}(f) = \{f(x) : x \in \mathcal{X}\}$. Then for linear transformation $f(\mathbf{x}) = \boldsymbol{M}\mathbf{x}$ with $\boldsymbol{M} \in \mathbb{R}^{d\times n}$, $\mathrm{Im}(f) = \{\boldsymbol{M}\mathbf{x} : \mathbf{x} \in \mathbb{R}^n\}$; we denote this as $\mathrm{Im}(\boldsymbol{M})$. Now, for any $g \in \mathcal{G}_d$, $\mathrm{Im}(g) = \{\boldsymbol{B} f(\boldsymbol{A}\mathbf{x}) : \mathbf{x} \in \mathbb{R}^n\} \subseteq \{\boldsymbol{B}\mathbf{y} : \mathbf{y} \in \mathbb{R}^d\} = \mathrm{Im}(\boldsymbol{B})$. Since $\mathrm{rank}(\boldsymbol{B}) \leq d$, $\dim \mathrm{Im}(g) \leq \mathrm{rank}(\boldsymbol{B}) \leq d < n$, therefore $\mathrm{Im}(g) \subseteq \mathrm{Im}(\boldsymbol{B}) \subset \mathbb{R}^n$.

Now, given $g \in \mathcal{G}_d$ and the deterministic pair $(\mathbf{x}_t, \mathbf{y}, t) \in (\mathbb{R}^n, \mathbb{R}^n, [0,1])$, by Projection Theorem,

$$\|g(\mathbf{x}_t, t) - \mathbf{y}\|^2 \geq \|\mathbf{u}_g - \mathbf{y}\|^2 \tag{3}$$

where $\mathbf{u}_g \in \mathrm{Im}(g)$ is the unique minimizer and $\mathbf{u}_g - \mathbf{y}$ is orthogonal to $\mathrm{Im}(g)$. Since $\|\cdot\|^2 \geq 0$, we can take expectation on both sides

$$\begin{aligned}
\inf_{g\in\mathcal{G}_d} \mathbb{E}_{\mathbf{x}\sim p(\mathbf{x}), \boldsymbol{\varepsilon}\sim\mathcal{N}(0,\mathbf{I}_n)} \left[\|g(\mathbf{x}_t, t) - \mathbf{y}\|^2\right] &\geq \inf_{g\in\mathcal{G}_d} \mathbb{E}\left[\|\mathbf{u}_g - \mathbf{y}\|^2\right] \\
&\geq \inf_{\mathbf{u}\in S; \dim S \leq d} \mathbb{E}\left[\|\mathbf{u} - \mathbf{y}\|^2\right] \\
&\geq \inf_{S; \dim S \leq d} \mathbb{E}\left[\|\mathbf{y}\|^2 - \|\boldsymbol{P}_S \mathbf{y}\|^2\right]
\end{aligned} \tag{4}$$

[1] family of functions $f : [0,1] \times \mathbb{R}^n \to \mathbb{R}^n$ that is continuous in t for all $(\mathbf{x}, t) \in [0,1] \times \mathbb{R}^n$, and $f(\cdot, t)$ is a continuously differentiable function from $\mathbb{R}^n$ to $\mathbb{R}^n$.

where $\boldsymbol{P}_S$ denote the projection matrix from $\mathbb{R}^n$ onto S. Without loss of generality, we assume $\mathbb{E}[\mathbf{x}] = 0$[2], then Eq 4 can be expanded as

$$\begin{aligned}\inf_{g\in\mathcal{G}_d} \mathbb{E}_{\mathbf{x}\sim p(\mathbf{x}),\boldsymbol{\varepsilon}\sim\mathcal{N}(0,\mathbf{I}_n)}\left[\|g(\mathbf{x}_t,t)-\mathbf{y}\|^2\right] &\geq \sum_{i=1}^{n}\mathbb{E}[\mathbf{y}_i^2] - \sup_{S;\dim S\leq d}\sum_{i=1}^{n}\mathbb{E}[(\boldsymbol{P}_S\mathbf{y})_i^2] \\ &= \mathrm{Tr}(\mathrm{Cov}(\mathbf{y})) - \sup_{S;\dim S\leq d}\mathrm{Tr}(\mathrm{Cov}(\boldsymbol{P}_S\mathbf{y})) \\ &\geq \sum_{i=1}^{n}\lambda_i - \sum_{i=1}^{d}\lambda_i = \sum_{i=d+1}^{n}\lambda_i \end{aligned} \tag{5}$$

where Eq 5 is obtained via Ky-Fan Maximum Principle.

When $d \geq n$, $\sup_S \mathbb{E}[\|\boldsymbol{P}_S\mathbf{y}\|^2] = \mathbb{E}[\|\mathbf{y}\|^2]$, leading to a trivial lower bound in Eq 5, and $\mathcal{G}_d = C^0((C^1(\mathbb{R}^n))^n;[0,1])$. □

C.2 Proof of Lower Bound for Inference Loss

Theorem 2. *Consider the same setup as Theorem 1. Let $\mathbf{x}_1$ be the initial random variables in the sampling process, and*

$$\begin{aligned}\mathbf{x}_0 &= \mathit{ODE}(g, \mathbf{x}_1, 1\to 0)\\ \mathbf{x}_0^* &= \mathit{ODE}(f^*, \mathbf{x}_1, 1\to 0)\end{aligned}$$

where $\mathit{ODE}(f,\mathbf{x},t\to s)$ refers to any ODE solver that integrates f from time t to s using $\mathbf{x}$ as the initial condition. We further assume for any $(\mathbf{x},\mathbf{y},t)\in(\mathbb{R}^n,\mathbb{R}^n,[0,1])$, there exists constant $L>0$ such that

$$\|f^*(\mathbf{x},t) - f^*(\mathbf{y},t)\| \leq L\|\mathbf{x}-\mathbf{y}\|$$

then

$$\|\mathbf{x}_0^* - \mathbf{x}_0\| \geq \frac{1-e^{-L}}{L}\sum_{i=d+1}^{n}\lambda_i \tag{6}$$

Proof. We first define a forward ODE that integrates from $0\to 1$ $\mathbf{x}_{\overleftarrow{t}} := \mathbf{x}_{-t}$, and

$$\begin{aligned}\mathrm{d}\mathbf{x}_{\overleftarrow{t}} &= g(\mathbf{x}_{\overleftarrow{t}}, t)\mathrm{d}t\\ \mathrm{d}\mathbf{x}^*_{\overleftarrow{t}} &= f^*(\mathbf{x}^*_{\overleftarrow{t}}, t)\mathrm{d}t\end{aligned}$$

Then

$$\begin{aligned}\frac{\mathrm{d}}{\mathrm{d}t}\|\mathbf{x}^*_{\overleftarrow{t}} - \mathbf{x}_{\overleftarrow{t}}\| &= \|f^*(\mathbf{x}^*_{\overleftarrow{t}}, t) - g(\mathbf{x}_{\overleftarrow{t}}, t)\| \\ &\geq \|f^*(\mathbf{x}_{\overleftarrow{t}}, t) - g(\mathbf{x}_{\overleftarrow{t}}, t)\| - \|f^*(\mathbf{x}^*_{\overleftarrow{t}}, t) - f^*(\mathbf{x}_{\overleftarrow{t}}, t)\| \\ &\geq \|\Delta\| - L\|\mathbf{x}^*_{\overleftarrow{t}} - \mathbf{x}_{\overleftarrow{t}}\|\end{aligned} \tag{7}$$

where Δ denotes the approximation error to f^* for $g\in\mathcal{G}_d$. Applying Gronwall's Lemma, we have

$$\begin{aligned} e^{L\overleftarrow{t}}\|\mathbf{x}^*_{\overleftarrow{t}} - \mathbf{x}_{\overleftarrow{t}}\|\Big|_0^1 &\geq \int_0^t e^{Ls}\|\Delta\|\mathrm{d}s \\ \implies \|\mathbf{x}_0^* - \mathbf{x}_0\| = \|\mathbf{x}^*_{\overleftarrow{1}} - \mathbf{x}_{\overleftarrow{1}}\| &\geq \frac{(1-e^{-L})}{L}\sum_{i=d+1}^{n}\lambda_i \end{aligned} \tag{8}$$

where by Theorem 1, $\|\Delta\| \geq \sum_{i=d+1}^{n}\lambda_i$. □

[2]Non-centered $\mathbf{x}$ with $\mathbb{E}[\mathbf{x}] = \mu$ will additionally introduce $\|\mu\|^2 - \|\boldsymbol{P}_S\mu\|^2$ to the lower bound; we ignore this term since most data processing pipelines will center the data

Figure 7: **Reconstruction examples.** From left to right: input image, RAE (DINOv2-B), RAE (SigLIP2-B), RAE (MAE-B), SD-VAE. Zoom in for details.

D GUIDANCE

We primarily adopt AutoGuidance (Karras et al., 2025) as our guidance method, as it is easier to tune than CFG with interval (Ho & Salimans, 2022; Kynkäänniemi et al., 2024) and consistently delivers better performance. CFG is used only for the DiT-XL + DINOv2-S with guidance result reported in Table 7.

AutoGuidance. We adopt AutoGuidance (Karras et al., 2025) as our primary guidance method. The idea is to use a weaker diffusion model to guide a stronger one, analogous to the principle of Classifier-Free Guidance (CFG) (Ho & Salimans, 2022). We observe that weaker base models and shorter training epochs consistently yield better guidance. Accordingly, for all RAE experiments, we find it sufficient to employ the smallest variant of DiT^{DH}, namely DiT^{DH}-S, as the base model, using an early checkpoint at 20 training epochs. We sweep the guidance scale to optimize FID. Notably, training this base model costs only 0.06% of the compute required for the guided model (DiT^{DH}-XL trained for 800 epochs).

Classifier-Free Guidance. We also evaluate CFG (Ho & Salimans, 2022) on RAE. Interestingly, CFG without interval does not improve FID; in fact, applying it from the first diffusion step increases FID. With Guidance Interval (Kynkäänniemi et al., 2024), CFG can achieve competitive FID after careful grid search over scale and interval. However, on our final model (DiT^{DH}-XL with DINOv2-B), the best CFG result remains inferior to AutoGuidance. Considering both performance and tuning overhead, we adopt AutoGuidance as our default guidance method.

E RAE IMPLEMENTATION

E.1 ENCODER NORMALIZATION

For any given frozen representation encoders, we discard any [CLS] or [REG] token produced by the encoder, and keep the all of patch tokens. We then apply a layer normalization to each token independently, to ensure each token has zero mean and unit variance across channels. We note that all representation encoders we use adopt the standard ViT architecture (Dosovitskiy et al., 2021), which have already applied layer normalization after the last transformer block. Therefore, we only need to cancel the affine parameters of the layer normalization in representation encoders. This does not affect the representation quality of representation encoders, as it is a linear transformation.

Practical Notes. Specifically, we use DINOv2 with Registers (Darcet et al., 2025). Since DINOv2 only provides variants with $p_e = 14$, we interpolate the input images to 224×224 but set $p_d = 16$, ensuring the model still produces 256 tokens while reconstructing 256×256 images.

E.2 Decoder Training Details

Datasets. We primarily use ImageNet-1K for training all decoders. Most experiments are conducted at a resolution of 256×256. For 512-resolution synthesis without decoder upsampling, we train decoders directly on 512×512 images.

Decoder Architecture. The decoder takes the token embeddings produced by the frozen encoder takes the token embedding reconstructs them back into the pixel space using the same patch size as the encoder. As a result, it can generate images with the same spatial spatial resolution as the encoder's inputs input. Following He et al. (2021), we prepend a learnable [CLS] token decoder's input sequence and discard it after decoding.

Discriminator Architecture. We include the majority of our decoder training details in Table 12. We follow most of the design choices in StyleGAN-T (Sauer et al., 2023), except for using a frozen Dino-S/8 (Caron et al., 2021b) instead of Dino-S/16 as the discriminator. We found using Dino-S/8 stabilizes training and avoid the decoder to generate adversarial patches. We also remove the virtual batch norm in Sauer et al. (2023) and use the standard batch norm instead. All input is interpolated to 224×224 resolution before feeding into the discriminator.

Table 12: Training configuration for decoder and discriminator.

Component	**Decoder**	**Discriminator**
optimizer	Adam	Adam
max learning rate	2×10^{-4}	2×10^{-4}
min learning rate	2×10^{-5}	2×10^{-5}
learning rate schedule	cosine decay	cosine decay
optimizer betas	(0.5, 0.9)	(0.5, 0.9)
weight decay	0.0	0.0
batch size	512	512
warmup	1 epoch	1 epoch
loss	ℓ_1 + LPIPS + GAN	adv.
Model	ViT-(ViT-B, ViT-L, ViT-XL)	Dino-S/8 (frozen)
LPIPS start epoch	0	–
disc. start epoch	–	6
adv. loss start epoch	8	–
Training epochs	16	10

Losses. We set $\omega_L = 1.$ and $\omega_G = 0.75$. We use the same losses as in StyleGAN-T Sauer et al. (2023) for discriminator, and a GAN loss as in Esser et al. (2021). We also adopt the adaptive weight λ for GAN loss proposed in Esser et al. (2021) to balance the scales of reconstruction and adversarial losses. λ is defined as:

$$\lambda = \frac{\|\nabla_{\hat{x}} \mathcal{L}_{rec}\|}{\|\nabla_{\hat{x}} \, \mathrm{GAN}(\hat{x}, x)\| + \epsilon},$$

Augmentations. For data augmentation, we first resize the input image to 384×384 and then randomly crop to 256×256. We also apply differentiable augmentations with default hyperparameters in Zhao et al. (2020) before discriminator.

E.3 Visualizations

We present visualizations of reconstructions from different RAEs. As shown in Figure 7, all RAEs achieve satisfactory reconstruction fidelity.

F Diffusion Model Implementation

Datasets. We primarily use ImageNet-1K for training all decoders. Most experiments are conducted at a resolution of 256×256. For 512-resolution synthesis without decoder upsampling, we train diffusion models directly on 512×512 images.

Models. By default, we use LightningDiT (Yao et al., 2025) as the backbone of our diffusion model. We use a continuous time formulation of flow matching and restrict the timestep input to real values in $[0, 1]$. Following prior work (Song et al., 2021), we replace the timestep embedding with a Gaussian Fourier embedding layer. We also add Absolute Positional Embeddings (APE) to the input tokens in addition to RoPE, though we do not observe significant performance difference with or without APE.

Model Config	Dim	Num-Heads	Depth
S	384	6	12
B	768	12	12
L	1024	16	24
XL	1152	16	28
XXL	1280	16	32
H	1536	16	32
G	2048	16	40
T	2688	21	40

Table 13: Model configurations for different sizes.

For DiT^{DH}, we generally follow the same architecture as DiT, and does not reapply APE for the DDT head input. We use a linear layer to map the DiT^{DH} encoder output to the DiT^{DH} decoder dimension when the dimension of DiT and DDT head mismatches.

Patch Size. For all models on RAE, we use a patch size of 1. For baselines experiments on VAE and pixel, we use a patch size of 2 and 16, respectively. For all 256×256 experiments, the diffusion accepts a token sequence length of 256.

Optimization. For DiT, we strictly follow the optimization strategy in LightningDiT (Yao et al., 2025), using AdamW with a constant learning rate of 2.0×10^{-4}, a batch size of 1024 and an EMA weight of 0.9999. We do not observe instability or abnormal training dynamics with this recipe on DiT. For DiT^{DH}, we found using the recipe in (Yao et al., 2025) leads to loss spikes at later epochs and slow EMA model convergence at early epochs. We instead use a linear decay from 2.0×10^{-4} to 2.0×10^{-5} with a constant warmup of 40 epochs. To encourage the convergence of EMA model, we change the EMA weight from 0.9999 to 0.9995. Other optimization hyperparameters are the same as DiT. All models are trained for 80 epochs unless otherwise specified. We only report EMA model performance.

Sampling. We use standard ODE sampling with Euler sampler and 50 steps by default. We find the performance generally converges above 50 steps. We use the same sampling hyperparameters for both DiT and DiT^{DH}.

G Theory Experiment Setup

In this section we list the setup of experiments in Section 4 for overfitting images.

Models. By default, we use a DiT with depth 12, width 768 and a attention head of 4. The depth varies in $\{384.512, 640, 768, 896\}$ and width varis in $\{4, 12, 16, 24\}$ in Figure 3. Other configurations are the same as Appendix F.

Targets. We use three images for overfitting experiments, and all numbers reported are the average on three independent run on each images. We do resize all targets to 256×256 and not use any data augmentation .

Optimizations & Sampling. For a single target image, the batch size only influences the timestep. We therefore use a relatively small batch size of 32 and a constant learning rate of 2×10^{-4}, optimized with AdamW ($\beta = (0.9, 0.95)$). The model is trained for 1200 steps without EMA. For sampling, We use standard ODE sampling with Euler sampler and 25 steps by default.

(a) gFID and rFID of different encoders w/ and w/o noisy-robust decoding.

Model	gFID	rFID
DINOv2-B	4.81 / 4.28	0.49 / 0.57
SigLIP2-B	6.69 / 4.93	0.53 / 0.82
MAE-B	16.14 / 8.38	0.16 / 0.28

(b) gFID and rFID of different DINOv2 sizes w/ and w/o noisy-robust decoding.

Model	gFID	rFID
S	3.83 / 3.50	0.52 / 0.64
B	4.81 / 4.28	0.49 / 0.57
L	6.77 / 6.09	0.52 / 0.59

(c) Scaling τ for DINOv2-B.

τ	gFID	rFID
0.0	4.81	0.49
0.5	4.39	0.54
0.8	4.28	0.57
1.0	4.20	0.60

Table 14: **Ablations on noise-augmented decoder training.** Despite minor drop in rFID, the noise-augmented training strategy can greatly improve the gFID across different encoders and model sizes.

H Additional Ablation Studies

H.1 Generation Performance across Encoders

As shown in Table 14a, DINOv2-B achieves the best overall performance. MAE performs substantially worse in generation, despite yielding much lower rFID. This shows that a low rFID does not necessarily imply a good image tokenizer. Therefore, we use DINOv2-B as the default encoder for our image generation experiments.

H.2 Design choices for noise-augmented decoding

We first analyze how noise-robust decoding affects reconstruction and generation. Table 14c shows that larger τ improves generative FID (gFID) consistently, but slightly worsens reconstruction FID (rFID). This supports our intuition: noise encourages the decoder to learn smoother mappings that generalize better to imperfect latents, improving generation quality, but reducing exact reconstruction accuracy.

To test the robustness of this trade-off, we evaluate different encoders (Table 14a) with $\sigma = 0.8$. Across all encoders, noisy training improves gFID while mildly harming rFID. The effect is strongest for weaker encoders such as MAE-B, where gFID improves from 16.14 to 8.38. Finally, Table 14b shows that the benefit holds across encoder sizes, suggesting that robust decoder training is broadly applicable.

Together, these results highlight a general principle: decoders should not only reconstruct clean latents, but also handle their noisy neighborhoods. This simple change enables RAEs to serve as stronger backbones for diffusion models.

H.3 Design Choices for the DDT Head

Depth	Width	GFLops	FID ↓
6	1152 (XL)	25.65	2.36
4	2048 (G)	53.14	2.31
2	2048 (G)	26.78	2.16

Table 15: **DDT head needs to be wide and shallow.**

	2-768	2-1536	2-2048	2-2688
Dino-S	2.66	2.47	2.42	2.43
Dino-B	2.49	2.24	2.16	2.22
Dino-L	N/A	2.95	2.73	2.64

Table 16: **Unguided gFID of different RAE and DDT head.** Larger RAE benefits more from wider DDT head. d-w: a DDT head with d layers and width w.

We now investigate design variants of the DDT head to identify those that serve its role more effectively. Two factors turn out to be crucial: (a) the head needs to be wide and shallow, and (b) its benefit depends on the size of the underlying RAE encoder.

Width and Depth. We first vary the architecture of the DDT head, sweeping both width and depth while keeping the total parameter count approximately fixed. As shown in Table 15, a 2-layer, 2048-dim (G) head outperforms a 6-layer, 1152-dim (XL) head by a large margin, despite having similar

GFlops. Moreover, a 4-layer, 2048-dim head does not improve over the 2-layer version, even though it has double the GFlops. This suggests that a wide and shallow head is more effective for denoising.

Dependence on Encoder Size. Next, we analyze how the effect of the DDT head scales with the size of the RAE encoder. We fix the DiT backbone as DiT-XL and vary the DDT head width from 768 (B) to 1536 (H), 2048 (G), and 2688 (T). We train DiT$^{\text{DH}}$ models on top of three RAEs: DINOv2-S, DINOv2-B, and DINOv2-L. As shown in Table 16, the optimal DDT head width increases as the encoder scales. When using DINOv2-S and DINOv2-B, the performance converges at a DDT head width of 2048 (G), while 2688 (T) head still brings performance gains on DINOv2-L. This suggests that the larger RAE encoders benefit more from a wider DDT head.

By default, we use a 2-layer, 2048-dim DDT head for all DiT$^{\text{DH}}$ models in the rest of the paper.

I Descriptions for Flow-based Models

Diffusion Models (Ho et al., 2020; Dhariwal & Nichol, 2021; Karras et al., 2022) and more generally flow-based models (Albergo et al., 2023; Lipman et al., 2023; Liu et al., 2023) are a family of generative models that learn to reverse a reference "noising" process. One of the most commonly used "noising" process is the linear interpolation between i.i.d Gaussian noise and clean data (Esser et al., 2024; Ma et al., 2024):

$$\mathbf{x}_t = (1-t)\mathbf{x} + t\boldsymbol{\varepsilon}$$

where $\mathbf{x} \sim p(\mathbf{x}), \boldsymbol{\varepsilon} \sim \mathcal{N}(0, \mathbf{I}_n), t \in [0,1]$, and we denote $\mathbf{x}_t$'s distribution as $\rho_t(\mathbf{x})$ with $\rho_0 = p(\mathbf{x})$ and $\rho_1 = \mathcal{N}(0, \mathbf{I})$. Generation then starts at $t = 1$ with pure noise, and simulates some differential equation to progressively denoise the sample to a clean one. Specifically for flow-based models, the differential equations (an ordinary differential equation (ODE) or a stochastic differential equation (SDE)) are formulated through an underlying velocity $v(\mathbf{x}_t, t)$ and a score function $s(\mathbf{x}_t, t)$

$$\begin{aligned} \text{ODE} \quad & \mathrm{d}\mathbf{x}_t = v(\mathbf{x}_t, t)\mathrm{d}t \\ \text{SDE} \quad & \mathrm{d}\mathbf{x}_t = v(\mathbf{x}_t, t)\mathrm{d}t - \frac{1}{2} w_t s(\mathbf{x}_t, t)\mathrm{d}t + \sqrt{w_t}\mathrm{d}\bar{\mathbf{w}}_t \end{aligned}$$

where w_t is any scalar-valued continuous function (Ma et al., 2024), and $\bar{\mathbf{w}}_t$ is the reverse-time Wiener process. The velocity $v(\mathbf{x}_t, t)$ is represented as a conditional expectation

$$v(\mathbf{x}_t, t) = \mathbb{E}[\dot{\mathbf{x}}_t | \mathbf{x}_t] = \mathbb{E}[\boldsymbol{\varepsilon} - \mathbf{x} | \mathbf{x}_t]$$

and can be approximated with model v_θ by minimizing the following training objective

$$\mathcal{L}_{\text{velocity}}(\theta) = \int_0^1 \mathbb{E}_{\mathbf{x}, \boldsymbol{\varepsilon}} \Big[\| v_\theta(\mathbf{x}_t, t) - (\boldsymbol{\varepsilon} - \mathbf{x}) \|^2 \Big] \mathrm{d}t$$

The score function $s(\mathbf{x}_t, t)$ is also represented as a conditional expectation

$$s(\mathbf{x}_t, t) = -\frac{1}{t}\mathbb{E}[\boldsymbol{\varepsilon} | \mathbf{x}_t]$$

Notably, s is equivalent to v up to constant factor (Albergo et al., 2023), so it's enough to estimate only one of the two vectors.

J Evaluation Details

J.1 Evaluation

We strictly follow the setup and use the same reference batches of ADM (Dhariwal & Nichol, 2021) for evaluation, following their official implementation.[3] We use TPUs for generating 50k samples and use one single NVIDIA A100 80GB GPU for evaluation.

In what follows, we explain the main concept of metrics that we used for the evaluation.

[3] https://github.com/openai/guided-diffusion/tree/main/evaluations

- **FID** (Heusel et al., 2017) evaluates the distance between the feature distributions of real and generated images. It relies on the Inception-v3 network (Szegedy et al., 2016) and assumes both distributions follow multivariate Gaussians.
- **IS** (Salimans et al., 2016) also uses Inception-v3, but evaluates logits directly. It measures the KL divergence between the marginal label distribution and the conditional label distribution after softmax normalization.
- **Precision and recall** (Kynkäänniemi et al., 2019) follow their standard definitions: precision reflects the fraction of generated images that appear realistic, while recall reflects the portion of the training data manifold covered by generated samples.

K Unconditional Generation

We are also interested in how RAEs perform in unconditional generation. To evaluate this, we train DiT^{DH}-XL on RAE latents without labels. Following RCG (Li et al., 2024a), we set labels to null during training and use the same null label at generation time. While classifier-free guidance (CFG) does not apply in this setting, AutoGuidance remains applicable. We therefore train DiT^{DH}-XL for 200 epochs with AG (detailed in Appendix D).

As shown in Table 17, our model achieves substantially better performance than DiT-XL trained on VAE latents. Compared to RCG, a method specifically designed for unconditional generation, our approach attains competitive performance while being much simpler and more straightforward, without the need for two-stage generation.

Method	gFID ↓	IS ↑
DiT-XL + VAE	30.68	32.73
DiT^{DH}-XL + DINOv2-B (w/ AG)	4.96	123.12
RCG + DiT-XL	4.89	143.2

Table 17: **Comparison of unconditional generation on ImageNet 256 × 256.**

L Visual Results

We show uncurated 512 × 512 samples sampled from our most performant model: DiT^{DH}-XL on DINOv2-B with autoguidance scale = 1.5.

Figure 8: **Uncurated** 512×512 **DiT^{DH}-XL samples.**
AutoGudance Scale = 1.5
Class label = ”golden retriever” (207)

Figure 9: **Uncurated** 512×512 **DiT^{DH}-XL samples.**
AutoGudance Scale = 1.5
Class label = ”husky” (250)

Figure 10: **Uncurated** 512×512 **DiT^{DH}-XL samples.**
AutoGudance Scale = 1.5
Class label = ”cliff” (972)

Figure 11: **Uncurated** 512×512 **DiT^{DH}-XL samples.**
AutoGudance Scale = 1.5
Class label = ”macaw” (88)

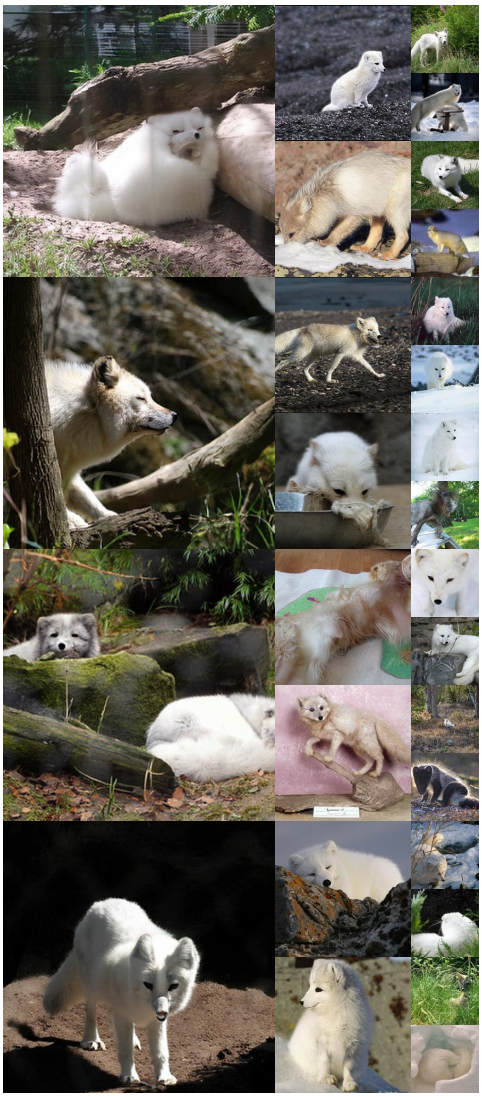

Figure 12: **Uncurated** 512×512 **DiT$^{\text{DH}}$-XL samples.**
AutoGudance Scale = 1.5
Class label = ”arctic fox” (279)

Figure 13: **Uncurated** 512×512 **DiT$^{\text{DH}}$-XL samples.**
AutoGudance Scale = 1.5
Class label = ”balloon” (417)

Method	Compute@256						Compute@512					
	AE		Diffusion		Wall-clock	gFID	AE		Diffusion		Wall-clock	gFID
	Param.	GFlops	Param.	GFlops			Param.	GFlops	Param.	GFlops		
Latent Diffusion with SD-VAE												
SiT (Ma et al., 2024)			675M	118.64	8.88 steps/sec	2.06			675M	524.60	2.49 steps/sec	2.62
REPA (Yu et al., 2025)	84M	445.87	675M	118.64	8.88 steps/sec	1.42	84M	1783.49	675M	524.60	2.49 steps/sec	2.08
DDT (Wang et al., 2025c)			675M	118.64	8.12 steps/sec	1.26			675M	508.46	2.31 steps/sec	1.25
Latent Diffusion with RAE (Ours)												
DiT^{DH}-XL (DINOv2-B)	501M	129.02	839M	145.03	7.20 steps/sec	1.13	501M	513.57	839M	638.83	2.07 steps/sec	1.13
DiT^{DH}-XL (DINOv2-B, Upsampling)	-	-	-	-	-	–	503M	129.70	839M	129.02	7.20 steps/sec	1.61

Table 18: **Compute comparison.** Wall-clock numbers are measured end-to-end on identical hardware.

M Computation Costs

In this section, we compare the computational costs of RAE-based and VAE-based models in terms of GFLOPs, parameter counts, and wall-clock training time. We report the per-forward GFLOPs for each model, as backward and total training GFLOPs scale proportionally. Wall-clock time is measured end-to-end without latent caching on identical hardware (a v5p-128 TPU Pod utilizing a JAX codebase). We note that due to hardware differences, absolute timings on GPUs may vary.

As shown in Table 18, RAE requires $3.5\times$ fewer GFLOPs than SD-VAE at both 256 and 512 resolutions. While DiT^{DH}-XL incurs approximately 22% more GFLOPs than the DiT-XL baseline (on SD-VAE) due to the overhead of the DDT Head—resulting in slower training times—the use of decoder upsampling offers significant gains. Specifically, DiT^{DH}-XL on DINOv2-B achieves a $13.8\times$ reduction in GFLOPs for the autoencoder and a $4.1\times$ reduction for diffusion, all while maintaining competitive FID scores compared to VAE-based baselines.

N Text-to-image Synthesis with RAE

To rigorously evaluate the scalability and generalizability of the proposed RAE, we extend our investigation to the domain of text-to-image (T2I) generation. Although still in progress, preliminary experimental results provide strong evidence that the architectural advantages of RAE over standard VAEs persist in generative settings beyond ImageNet.

N.1 Training RAE on webimages

We first extend RAE decoder training to web-scale images to investigate the generalizability and scalability of the model. By default, we employ SigLIP2 ViT-So (Tschannen et al., 2025), a prevalent choice for large-scale multimodal encoding, as our RAE encoder. We also experiment with webSSL ViT-L (Fan et al., 2025a), a DINOv2 variant pre-trained on general web images. We re-tune our GAN training recipe for the web data regime and, for comparison, train a separate decoder for SigLIP2 ViT-So on ImageNet. We report both quantitative (rFID, PSNR, SSIM) and qualitative results. We evaluate the reconstruction performance on ImageNet validation set and a 50k subset drawn from YFCC (Thomee et al., 2016), a webimage dataset.

Family	Model	ImageNet			YFCC		
		rFID ↓	PSNR ↑	SSIM ↑	rFID ↓	PSNR ↑	SSIM ↑
VAE	SD-VAE	0.978	24.78	0.705	0.987	25.25	0.738
	FLUX	0.288	30.92	0.894	0.410	32.18	0.920
RAE	DINOv2-L*	0.388	22.18	0.637	0.556	22.52	0.669
	SigLIP2-So (IN)	0.462	20.82	0.563	0.970	20.95	0.591
	SigLIP2-So (Web)	0.435	21.34	0.593	0.702	21.75	0.628

Table 19: **Quantitative comparison of reconstruction performance.** We report rFID (↓), PSNR (↑), and SSIM (↑) on ImageNet and YFCC. '(IN)' denotes training on ImageNet, while others are trained on web-scale data. Default settings are marked in green. *: we use WebSSL (Fan et al., 2025a), a variant of DINOv2.

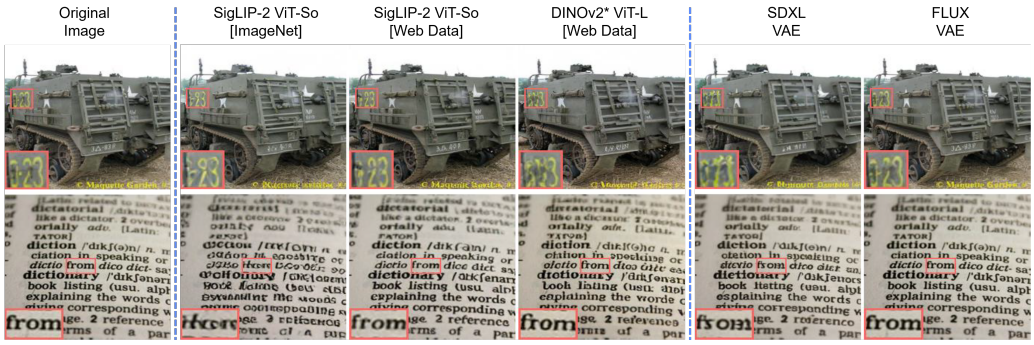

Figure 14: **RAE decoders trained on more data generalize across domains.** Decoders trained only on ImageNet reconstruct natural images well but struggle with text-rendering scenes. Training on webimages improves text reconstruction while maintaining natural-image quality. Compared to proprietary VAEs, our RAE achieves competitive overall fidelity. *: we use WebSSL (Fan et al., 2025a), a variant of DINOv2.

As shown in Figure 14, scaling the decoder training significantly mitigates reconstruction artifacts, particularly for text and small objects. The results in Appendix N.1 demonstrate that training on web images enhances the generalizability of RAE decoders for both in-domain (web images) and out-of-domain (ImageNet) reconstruction. Notably, the decoder trained on web images outperforms the ImageNet-trained counterpart even on ImageNet evaluation, suggesting that training on larger and more diverse data substantially improves general reconstruction capabilities. Although they still trail FLUX-VAE, both RAEs utilizing SigLIP2 and WebSSL outperform SDXL-VAE in rFID, demonstrating highly competitive reconstruction ability.

N.2 Training text-to-image models on RAE

Model Architecture. Following recent progress in T2I generation, we build upon the open-source MetaQuery (Pan et al., 2025) framework. Our instantiation uses a 1.5B-parameter Qwen2.5 LLM and a 2.4B-parameter DiT as the generative backbone. We employ SigLIP2 ViT-So as the RAE encoder together with our web-trained RAE decoder. Unlike MetaQuery, our setup initializes from a base LLM rather than a pretrained vision–language model.

Data. The training corpus consists of text–image pairs curated from open-source datasets used in fuseDiT (Tang et al., 2025a), augmented with synthetic images generated by FLUX (Labs, 2024). We additionally incorporate Cambrian7M (Tong et al., 2024) to better align RAE latents with the LLM.

Training. During training, the RAE is kept frozen; we jointly train the LLM, DiT, and lightweight adapters end-to-end. For VQA-style data, we compute a cross-entropy loss L_c, and for generation data we use a diffusion loss L_d. The total objective is

$$L = L_c + 2L_d.$$

Baselines. We compare against a strong VAE baseline by replacing the RAE tokenizer with FLUX-VAE—the state-of-the-art VAE used in modern T2I systems—while keeping all other components identical. Both models are trained for 30k steps with a global batch size of 2048.

N.3 Preliminary Results

Convergence. Empirical results highlight the efficiency of RAE in text-to-image synthesis. As illustrated in Figure 15, the RAE-based model exhibits significantly faster convergence than its VAE counterpart. Quantitatively, RAE achieves a **3.75× speedup** on GenEval and DPGBench, underscoring its computational efficiency and suitability for large-scale generative tasks.

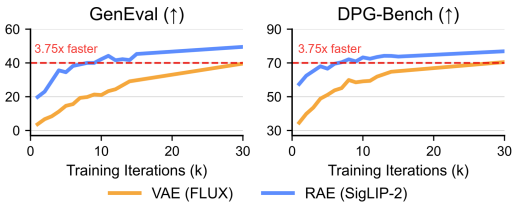

Figure 15: **RAE converges faster than VAE.** RAE achieves a **3.75× speedup** compared to the VAE counterpart.

Model	MME$_P$	TVQA	AI2D	Seed	MMMU	MMMU$_P$
Und.-only	1374.8	44.7	63.9	67.1	40.2	20.5
RAE-based	1468.7	39.6	66.7	69.8	41.1	19.8

Table 20: **Generative training leaves understanding intact.** Across VL benchmarks, the RAE-based model maintains performance comparable to the understanding-only baseline.

Figure 16: **RAE-based text-to-image model demonstrates strong prompt-following ability.** *Top*: generations without decoder upsampling (224 resolution). *Bottom*: generations with decoder upsampling to 378 resolution.

Decoder upsampling. As demonstrated in Section 6.1, we can directly leverage a generative model pretrained at low resolution for high-resolution synthesis via decoder upsampling. To validate the effectiveness of this approach for T2I, we train an upsampling decoder that increases the resolution from 224 to 378. As shown in Figure 16, the generated images are of high quality and maintain content consistency with their non-upsampled 224-resolution counterparts.

Image understanding. Since we utilize a base LLM without vision-language pretraining, the model's image understanding capability is determined jointly by the understanding and generation data used during end-to-end training. As shown in Table 20, our model exhibits understanding abilities comparable to a VQA-only baseline (where generation data is excluded). This indicates that within the RAE framework, the inclusion of generation data does not degrade understanding performance.

O Interpreting the diffusability of RAE via tSNE

A key remaining question is how the choice of RAE encoder influences generation performance. While we demonstrated in Appendix E.1 that the encoder choice dramatically impacts results, the underlying mechanism requires further explanation. We perform tSNE visualizations on the representations from various RAE encoders, using SD-VAE as a baseline. To extract features for visualization, we use the `[CLS]` token for encoders that possess one (MAE, DINOv2), and apply global pooling over all patch tokens for those that do not (SigLIP2, SD-VAE).

As illustrated in Figure 17, we observe a clear hierarchy in class separation: SD-VAE $<$ MAE $<$ SigLIP2 $<$ DINOv2. DINOv2 exhibits the most distinct clustering among classes, while MAE shows the least separation among the discriminative encoders, though it still surpasses SD-VAE. Intuitively, well-separated class clusters simplify the learning of the generative model; the class-

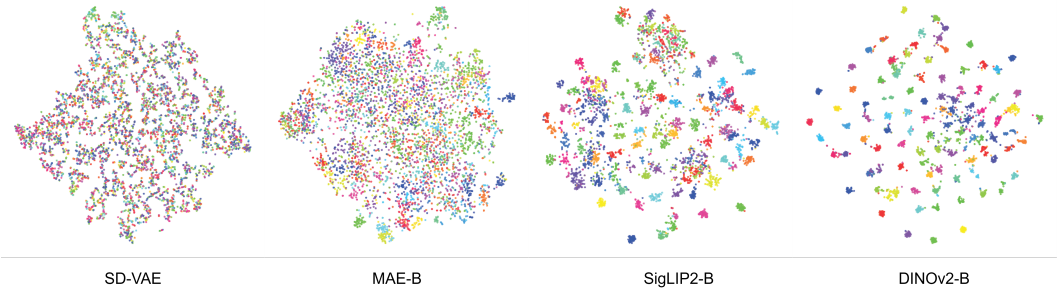

Figure 17: **tSNE examples.** We use 50 images per class from ImageNet validation set, and 100 classes for tSNE visualization.

Figure 18: **Noise-augmented decoding refines high-frequency details in generated images.** Zoom in for details.

conditioned velocity becomes more coherent within classes and distinct between them, making the diffusion process easier to fit.

P Additional Results

Qualitative samples of noise-augmented decoding. We provide visual examples illustrating the effect of noise-augmented decoding. As shown in Figure 18, noise-augmented decoding adds more high-frequency details to the generated images, resulting in improved FID and IS.

Training dynamics. We examine how model scale affects training loss in Figure 19. Increasing the model's computational capacity leads DiT^{DH} to converge faster and reach a lower final loss without loss spikes.

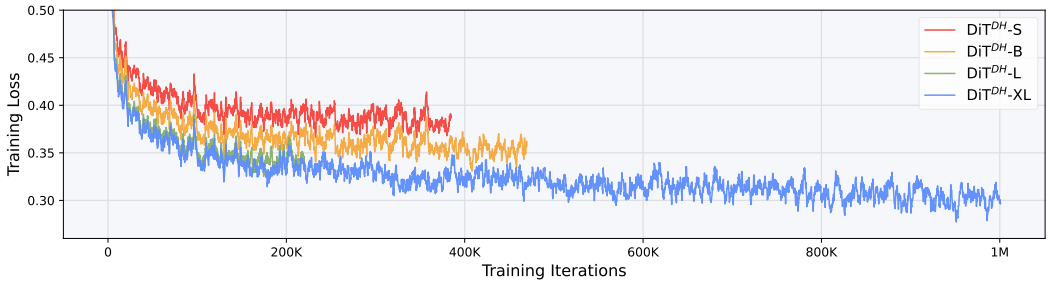

Figure 19: **Training loss of DiT^{DH} on DINOv2-B.** We use an EMA weight of 0.9 to smooth the loss. No loss spikes is observed during training.